Final Report - NEHRP

Award # G10AP00007

3D Broadband Ground Motion Estimation for Large Earthquakes on the New Madrid Seismic Zone, Central United States

1 January 2010 – 31 December 2011

Principal Investigators:*

Kim B. Olsen
Dept of Geological Sciences, San Diego State University,
5500 Campanile Dr, San Diego, CA 92182,
ph 619 594 2649, fax 619 594 4372
e-mail: kbolsen@sciences.sdsu.edu

* Jinquan Zhong also contributed significantly to the work reported here

Abstract

We predict ground motions in the New Madrid Seismic Zone (NMSZ) during M_w7.4-7.7 earthquakes on three different fault segments believed to have generated the enigmatic 1811-1812 events, using the Central United States velocity model version 1.2 (cusvm1.2, Ramirez-Guzman et al., 2012). The results are obtained as a coordinated effort though a working group between USGS-Golden and Memphis, URS, SDSU, and CERI. Our comparison of 0-1Hz synthetics versus recorded seismic data for the 2008 M_w5.2 Mt Carmel, IL, earthquake using the 3D crustal structure shows a generally good fit in the NMSZ area and vicinity. For the ground motion predictions, we first generated a suite of realistic source representations by simulating spontaneous rupture process on a planar, vertical fault with the staggered-grid split-node finite difference method. The initial distribution of shear stress is the sum of both a regional depth-dependent shear stress appropriate for an either dipping or vertical fault, and a stochastically generated residual shear stress field associated with previous ruptures. The slip rate histories from the spontaneous rupture scenarios are then projected onto the three segments of the NMSZ: two vertical segments with right-lateral strike-slip mechanism (the SW segment - a 140 km long by 22 km wide segment, and the NE segment: a 70 km long by 22 km wide segment), and a 60 km long by 40 km wide dipping segment with thrust mechanism (the central segment). Next we simulate 0-1 Hz wave propagation from nine dynamic source models with a 3D finite difference code, in the cusvm1.2, and generate broadband (BB, 0-10 Hz) ground motions for the earthquake scenarios in the NMSZ, by combining the 0-1 Hz finite-difference synthetics with high-frequency (1-10 Hz) S-to-S back-scattering operators.

Our results show that horizontal spectral accelerations at two seconds (2s-SAs) reveal strong rupture directivity effects, in particular for unilateral but also bi-lateral ruptures, as well as significant amplifications by the low-velocity sediments in the Mississippi Embayment. The largest peak ground velocities (PGVs), peak ground accelerations (PGAs), and peak spectral accelerations (SAs) are found on or immediately next to the fault traces. Out of the major urbanized areas in the region, Memphis experiences the largest long-period peak ground motions, while the values for St Louis, MO and Evansville, IN, are much smaller. Combined with a duration of the shaking of up to 30-40 seconds, these worst-case scenarios could inflict sizable damage on the built environment. A M_w7.7 event on the southwest segment with bi-lateral or north-south rupture direction tend to generate the largest ground motions (PGVs up to ~5 cm/s and SAs up to ~0.5g) in Memphis. Peak ground motions in St Louis and Evansville (<0.1g and PGVs below ~2 cm/s) will be felt, but likely not generate significant damage from any of the NMSZ scenarios.

Bibliography of all publications resulting from the work performed under the award

Ramirez-Guzman, L., Graves, R.W., Olsen, K.B., Boyd, O.S., Hartzell, S., Ni, S., Somerville, P.G., Williams, R.A., Zhong, J. (2011). Central United States earthquake ground motion simulation working group: the 1811-1812 New Madrid earthquake sequence. *Seismol. Research Letters,* **82**, No. 2, 275.

Ramirez Guzman, L., Graves, R.W. Olsen, K.B. Boyd, O.S. Hartzell, S., Ni, S., Somerville, P.G., Williams, R.A., and Zhong, J. (2011). Magnitude Uncertainty and Ground Motion Simulations of the 1811-1812 New Madrid Earthquake Sequence. Abstract *S22A-07* Presented at 2011 Fall Meeting, AGU, San Francisco, CA, 2011.

Final Technical Report

Background

On 16 December 1811, 23 January 1812, and 7 February 1812, three of the largest earthquakes reported in the continental United States occurred near the town of New Madrid, Missouri, in the Mississippi Embayment. The magnitudes of the events are uncertain, but were estimated at M_I 7.5-7.8 by Bakun and Hopper (2004). There are numerous studies of the possible sources of the earthquakes (e.g., Bakun and Hopper, 2004; Hough et al., 2000; Johnston, 1996), with several suggested candidate rupture segments (see Figure 1). The region, in particular the town of New Madrid, suffered great damage from the 1811-1812 earthquake sequence. The recurrence time of such events is estimated to be between 200 and 800 years, with an average of about 500 years (Tuttle et al., 2002). Thus, we are at the beginning of a period where such large events are expected to repeat themselves, and an assessment of the seismic hazards related to such earthquakes is appropriate.

One of the biggest uncertainties regarding earthquake hazards in the central US, and in particular for repeats of the 1811-1812 events, is the extent to which the basin sediments in the Mississippi Embayment will amplify seismic waves. It is well known that amplification of ground motion at sites underlain by deep and/or soft unconsolidated material can be a major contributor to the loss of life and property during earthquakes. Recent dramatic examples include the devastation caused in Mexico City by the 1985 M_w 8.1 Michoacan, Mexico, earthquake, despite the fact that the nearest point of the fault rupture was 300 km away (Anderson et al., 1986), and the severe damage caused by the 1989 M 7.0 Loma Prieta, California, earthquake in the cities of San Francisco and Oakland at distances of 60 to 70 km from the nearest point of the fault rupture (U.S. Geological Survey Staff, 1990). In both cases, resonances within low-impedance near-surface sediments served to amplify low frequency ground motions and add considerably to the damage (Anderson et al., 1986; Singh et al., 1988; Hough et al., 1990).

Even the fastest supercomputers available today cannot deterministically simulate ground motion for the whole 0-10 Hz frequency range that is relevant for engineering. For this reason broadband (BB) methods have been developed which combine deterministic low-frequency (LF) ground motions with a high-frequency (HF) component to generate synthetic seismograms for the entire frequency range of engineering interest. A number of methods use stochastic seismograms to generate the HF component of the signal (Graves and Pitarka, 2010; Mena et al., 2006). Other methods incorporate the physics of wave scattering at frequencies above 1 Hz to simulate the HF ground motions (Zeng et al., 1995; Hartzell et al., 2005). Mai et al. (2010) combined HF (1-10 Hz) S-to-S back-scattering seismograms with LF (0-1 Hz) deterministic seismograms for the 1994 Northridge earthquake, and found that the resulting broadband synthetics were consistent with observations for the modeled frequency range. Mena et al. (2010) developed the method further by incorporating dynamically consistent source-time functions and accounting for finite-fault effects in the computation of the HF waveforms. Their method also includes corrections for local site effects that use frequency- and amplitude-dependent amplification functions (Borcherdt, 1994); more recently, Campbell and

Bozorgnia (2008) presented updated frequency- and amplitude-dependent site correction functions, which are used in this project.

It is imperative to gain a solid understanding of the expected ground motions from future large earthquakes in the New Madrid region so that structures in the area can be properly engineered to withstand this shaking. In this report we present 3D broadband simulations of large (M_w7.4-7.7) earthquake scenarios on the New Madrid seismic zone (NMSZ) generated on a parallel supercomputer. We use the hybrid method by Mai et al. (2010) to generate BB synthetics in a 400 km (E-W) by 560 km (N-S) area by combining 0-1Hz FD LF synthetics with source descriptions based on dynamic rupture propagation, and HF (1-10Hz) scattering functions.

The simulations reported here are based on fault parameters defined in a collaboration between USGS-Golden and Memphis (O. Boyd, S. Hartzell, L. Ramirez-Guzman, and R. Williams), URS/USGS-Pasadena (S. Ni, P. Somerville, and R. Graves), SDSU (K. Olsen and J. Zhong), and CERI (H. DeShon, C. Cramer, C. Powell, and S. Horton).

Community Velocity Model for the Central USA and NMSZ Fault Geometry

We have used the 3-D Community Velocity Model version 1.2 (cusvm1.2, Ramirez-Guzman et al., 2012, in review). This model (see Figure 1) has been assembled from existing near-surface data including lithologic, density, and sonic logs, S-wave velocity measurements, and seismic reflection lines. The cusvm includes the lateral heterogeneity of the Mississippi embayment structure (Mooney *et al.*, 1983; Dart and Swolfs, 1998) based on the drill-hole data (Dart, 1992) and COCORP deep reflection profiles (Nelson and Zhang, 1991), as well as available geotechnical data. The principal feature of the Mississippi Embayment crust is the uplift of the deep crustal layers and the thinning of the upper crust. Seismic refraction studies by USGS in 1980 in the northern embayment (Mooney *et al.*, 1983; Ginzsburg *et al.*, 1983) contain the variation of deep crustal structure of the northern Mississippi Embayment. Features of the shallow structure such as the sub-basins, and major and minor structural highs that lie within upper and lower intra-rift basins are also included in the cusvm1.2 of the embayment structure. Anelastic attenuation was modeled using the Q_s-V_s relations listed in Table 1, along with Q_p=2Q_s.

Table 1. Q_s relations used in the simulations

V_s Range	Q_s Range
$V_s \leq 350$ m/s	35
350 m/s < $V_s \leq 500$ m/s	0.1 V_s
500 m/s < $V_s \leq 1000$ m/s	0.3 V_s - 100
1000 m/s < $V_s \leq 4000$ m/s	0.167 V_s + 33
400 < V_s	700

(Leonardo Ramirez-Guzman, Personal Communication, 2011).

We have tested and assessed the accuracy of the velocity model by performing numerical simulation of the 2008 M_w5.2 Mt Carmel, Illinois, earthquake, and compared the results

to recorded ground motions at 14 selected stations located throughout our simulation area (see Figure 2). The source parameters are listed in Table 2. We used a point source with sliprate function described in Hartzell and Mendoza (2011).

Table 2. Fault parameters 2008 Mt. Carmel used by USGS Golden-Memphis

Event Geographic Location	Lat. (North)	Lon. (West)	Depth (km)	Mw	Strike/Dip/ Rake
Mt. Carmel, Illinois	38.45	87.89	11	5.2	25/ 90 / -176

The comparisons are shown in Figure 3. Both synthetics and data are bandpass filtered between 0.1 and 1 Hz. Figure 3 shows a generally good fit in peak amplitude between the synthetics and data. The duration is modeled well for most stations, including the Mississippi Embayment near Memphis (e.g., stations CVTN, MKAR and CUET). However, the 0.1-1Hz duration is underpredicted in the northern part of the Embayment (stations HICK, PARM, PVMO, LNXT and GSAR) and just north of the Embayment (station SIUC). This underprediction is likely due to omission of near-surface material with shear-wave velocities less than 500 m/s in the Mt Carmel simulation due to computational limitations. However, for the final broadband synthetics generated in this project, the omission of the near-surface low velocity material is partly corrected for using frequency-dependent site amplification factors.

Fault Geometry for NMSZ simulations

The fault orientations for the 1811-1812 scenarios were selected from alignment of recent seismicity. In order to specify the fault planes, the rough geometry given by Macpherson et al. (2010) was adjusted so that they aligned more or less with the seismicity. The geometry and dimensions of these 3 planes are given in Table 3.

Table 3. Fault parameters for 1811-1812 New Madrid scenarios

Segment	**Top center Lon.**	**Top center Lat.**	**Depth to top (km)**	**Length (km)**	**Width (km)**	**Strike (o)**	**Dip (o)**	**Rake (o)**	**M_w**
Northeast	-89.35	36.875	1.0	70	22	215	90	180	7.4
Central	-89.40	36.370	1.0	60	40	155	38	90	7.6
Southwest	-89.95	35.950	1.0	140	22	225	90	180	7.7

The moment magnitude for each scenario is based on the magnitude-rupture area relation developed for stable continental regions by Somerville et al. (2009), $M_w = 4.35 + \log_{10}$ (Area).

Dynamic Rupture Modeling

In order to obtain a suite of realistic rupture models of M_w7.4-7-7 earthquakes in the NMSZ we perform simulations of spontaneous rupture on the three segments listed in Table 3 with the staggered-grid split-node FD method (Dalguer and Day, 2007). Because the code is limited to rupture simulation on a planar, vertical fault we adopt a two-step process. In a first step, we simulate the dynamic rupture process on a planar, vertical fault embedded in a 1-D model representative of the average crustal structure along the fault. Then the moment-rate time histories obtained from the spontaneous rupture simulation on the fault are projected onto the fault segments imbedded in the cusvm1.2, and we simulate the wave propagation resulting from the kinematic rupture models embedded in the heterogeneous 3D structure.

We generate 2 rupture scenarios for each of the three fault segments (the northeast, central and southwest segments) – a uni-lateral and a bi-lateral rupture. The uni-lateral rupture is later laterally mirrored to generate an additional rupture scenario. The dimension and location of the dynamic rupture models are summarized in Table 4.

Table 4. Dimensions and locations of the dynamic rupture models

Fault Segment	Fault Trace Upper End Points (lon, lat)	Epicenter (lon, lat)	Downdip Depth of Hypocenter (from fault Top (km)
Northeast	-89.5981,36.5414 -89.2599,37.1104	-89.4480,36.7951	16.3
		-89.5799,36.5723	18.4
		-89.2783,37.0795	18.4
Central	-89.2722,36.1310 -89.4945,36.6409	-89.6896,36.2742	35.5
		-89.6060,36.0650	36.3
		-89.8068,36.5216	36.3
Southwest	-90.5813,35.4732 -89.4434,36.3295	-90.0374,35.8860	14.7
		-90.5548,35.4935	18.5
		-89.4705,36.3094	18.5

We follow a method proposed by Dalguer et al. (2008) to define depth-dependent initial shear and normal stress (σ_n) on the fault. The failure stress ($\mu_f(z)$) on the fault obeys Coulomb friction and is defined as

$$\mu_f(z) = C + \mu_f \sigma'_n(z) = C + \mu_f (\sigma_n(z) + p),$$

where C is the cohesive strength of the fault, and p is the hydrostatic pressure, which

increases linearly with depth. The friction coefficient μ is described by a slip-weakening model:

$\mu(l) = \mu_s - (\mu_s - \mu_d)\, l/d_o$ if $l<d_o$, and $\mu(l) = \mu_d$ if $l \geq d_o$

where l is slip and d_o is the critical slip weakening distance. We used a cohesion C of 1 MPa, a static friction coefficient μ_s of 0.68 for the NE segment ruptures, 0.66 for the central segment ruptures, and 0.70 for the south-west segment ruptures, and a critical slip displacement d_o of 0.35 m for all ruptures. The dynamic friction coefficient μ_d was set to 0.55. This selection of parameters was found to generate generally sub-shear rupture propagation and slip distributions reasonable for M_w7.4-7.7 earthquakes in terms of the average and maximum slip (Wells and Coppersmith, 1994).

We generated a residual heterogeneous shear stress field τ_r (Ripperger et al., 2007) with a spectral decay that is compatible with seismological observations, using a fractal model with a correlation length of 5.5 km. Since the initial shear stress on the fault τ_0 is the combination of both the tectonic (τ_t) and residual stress components, we generated τ_0 by simply adding τ_t and τ_r so that its values are bounded by the static and dynamic fault strengths for all depths and such that the maximum shear stress reaches the static yield strength at a single point on the fault (Dalguer et al., 2008). Therefore, the location of the nucleation patch is predetermined by the location of the maximum in the random stress field. The initial shear stress was raised to 0.44% above the static failure stress inside the nucleation patch (diameter 3-6 km) in order to achieve stable sliding.

To emulate velocity strengthening in the shallow part of the crust d_o was increased from 0.2 m to 1.0 m in the top 4 km using a cosine taper. Similarly, μ_d was raised to a higher value than μ_s in the top 2 km of the crust, and tapered linearly between 2 km and 4 km depth. Additionally, the shear stress τ_0 was tapered to zero at the free surface starting at 2 km depth using a ramp function.

The spontaneous rupture simulations were performed on a mesh with a spatial discretization of 100 m, with a distance of 10 km from the fault to the nearest mesh boundary. Figures 4-6 show the final slip, rupture times and peak slip rates on the fault obtained for the three rupture segments. Little to no surface slip is generated, due to preventing the fault from breaking the top 1 km (in agreement with geological observations).

For each segment a uni-lateral rupture and a bi-lateral rupture are generated, with the hypocenter near the bottom of the fault. Then a 3rd source model is generated by laterally mirroring the uni-lateral rupture, in order to analyze the effects of different rupture directions on the resulting ground motions.

Kinematic Rupture Models

We generated nine kinematic source models from the spontaneous rupture simulation results. The three rupture scenarios for each fault segment consist of a bi-lateral rupture and two uni-lateral ruptures, where one of the latter is a lateral mirror of the other.

Broadband Ground Motions From NMSZ Scenario Earthquakes

We generated broadband (BB) synthetics for the nine kinematic sources using the hybrid approach by Mai et al. (2010) and Mena et al. (2010), combining low-frequency (LF) finite-difference (FD) synthetics with high-frequency (HF) scattering operators.

We simulated the LF wave propagation with the optimized, parallel AWP-ODC program (Cui et al., 2010), which is based on the 3D velocity-stress staggered-grid FD code developed by (Olsen, 1994). We used a computational regime of 400 km (E-W), 560 km (N-S) and 60 km (vertical), and the simulations were carried out to 4 minutes of wave propagation. With a minimum shear-wave velocity minimum V_s of 500 m/s and a grid step of 100 m, frequencies of up to 1.0 Hz can be modeled using at least 5 grid points per wavelength. Surface topography was not included in the wave propagation model. We used a coarse-grained implementation of the memory variables for a constant-Q solid (Day and Bradley, 2001) and Q relations listed in Table 1. The simulations were run on the kraken supercomputer at NICS using 7500 processors.

In the BB method of Mai et al. (2010) the generation of the HF part of the seismogram is based on multiple shear-to-shear (S-to-S) backscattering theory (Zeng et al., 1991). To generate a site-specific scattering Green's function, the code of Mai et al. (2010) generates a series of random scattering wavelets with uniformly distributed amplitudes between $\pm\sqrt{3}$, which assures a mean wave energy of unity (Zeng et al., 1995). These wavelets are then multiplied with the envelope of the scattered wave energy, with P- and S-wave arrival times for each site computed from a 3-D raytracing method. For the raytracer we used the same velocity model as for the 3-D FD simulations, downsampled to a spatial resolution of 1 km. Additionally, the code models site-specific attenuation in the upper layers with a kappa coefficient, κ, and a frequency-dependent attenuation relation. For our BB simulations in the NMSZ, we used a generic value of κ=0.04 s, and $Q_s(f)=150f^{0.8}$. Since the point source approximation by Mai et al. (2010) is not appropriate for modeling a $M_w > 7$ event on the WFSLC, we employ the extended fault approximation developed by Mena et al. (2010) for the generation of BB synthetics. We divide the NMSZ fault model into subfaults of 1 km^2 area each. The BB generator adds the contribution of each subfault to the total ground motion based on the empirical Green's function method of Irikura et al. (1994) and convolves the scattering Green functions with a smooth source time function including a healing phase (Dreger et al., 1997).

The LF FD synthetics are combined with the HF scatterograms (maximum frequency 20 Hz) using a simultaneous amplitude- and phase-matching algorithm (Mai and Beroza, 2003). This approach finds the optimum matching frequency within a predefined

frequency band and minimizes mismatches in both amplitude and phase. The matching frequency depends on the site and individual component. In this work we search for a matching frequency between 0.8 and 1.0 Hz, since our LF synthetics are limited to 1.0 Hz. We apply the scattering operators to LF synthetics at every 20th node on the surface of the computation grid. This results in a spatial resolution of 2 km and a grid dimension of 200 x 280 nodes (56,000 sites), which allows us to generate SA and PGA maps with sufficient resolution.

In order to incorporate amplification effects of the near-surface low-velocities not included in the FD simulations (where V_s^{min}=500 m/s), we applied the frequency- and amplitude dependent site correction factors by Campbell and Bozorgnia (2008).

Computation of peak ground motions

Here, we analyze the spatial distribution of resulting ground motions by computing SAs at periods of 2 s, 1 s, 0.33 s and 0.1 s, as well as PGAs and PGVs. To combine the response spectra of the two horizontal components into a single measurement of ground shaking, we use the orientation-independent measure GMRotD50 defined by Boore et al. (2006). The GMRotD50 value is obtained by calculating the geometrical mean of the two horizontal-component spectral accelerations for a range of rotation angles. The 2-s SAs are determined entirely by the LF FD seismograms, while the SAs at the shorter periods are controlled by both the LF and the HF components of the BB synthetics (since the HFs are scaled to the LFs by the hybrid method).

Analysis of peak ground motions

Figures 7-15 show GMrotD50 peak ground motions for selected SAs, PGAs and PGVs for all nine NMSZ scenarios. The largest SAs are found for the longest periods (SA-2s and SA-1s), as expected for the relatively large magnitude events modeled here. The largest SA-2s and SA-1s values are obtained for the M_w7.7 southwest segment ruptures, with accelerations up to about 3.5 g (2-s) and 2.5g (1-s), as well as the M_w7.6 central segment ruptures, with accelerations up to about 3g (2-s) and 2.5g (1-s). The deep hypocenter locations and thrust mechanism for these scenarios contribute to the relatively large peak motions. The smaller northeast segment ruptures (M_w7.4) generate SA-2s and SA-1s up to about 2g. SAs at shorter periods (e.g., 0.33s and 0.1s) as well as PGAs reach about 1.2-1.8g near the fault for the nine scenarios. Near-fault PGVs can exceed 50 cm/s for all scenarios, also largest for the central and southwest segment scenarios.

The scenarios show significant directivity effects, with larger peak motions in the direction of rupture propagation and a characteristic cone-shaped pattern with vertex at the epicenter for the vertical strike-slip events. Thus, the ground motion patterns are strongly dependent on the epicentral location. In addition, the central dipping segment tends to generate larger peak motions in the up-dip direction, due to directivity effects.

The effects of the heterogeneous dynamic rupture propagation is also apparent in the ground motion maps. A prominent example is the strong band of large SA-0.33s and

PGAs extending nearly perpendicularly out to 150 km or more from the fault at the end of the uni-lateral ruptures. These bands are generated by strong stopping phases, and the rupture terminates abruptly. Similarly, most other scenarios exhibit 'sun-bursts' of energy radiating from the fault, near locations where the rupture changes speed or direction over a short time frame.

The area affected by the largest peak motions is largest for the long period SAs (e.g., 2-s and 1-s), with significant amplitudes extending to 50-100 km from the fault trace (surface projection for the dipping central segment). This is in part dictated by the presence of the Mississippi Embayment with its relatively low near-surface shear-wave velocities. However, this area of influence is reduced significantly for the higher-frequency ground motion measures (e.g., SAs at 0.33s and 0.1s and PGAs).

Three major cities are located inside the simulation area: Memphis, St Louis, and Evansville (see Figure 1). Memphis, with a population exceeding 600,000 people, is the most exposed city in the area, due to its location inside the Mississippi Embayment and its close proximity to the NMSZ (< 50 km from the southwest segment). Memphis clearly experiences the strongest ground motions of the three population centers in the simulation area from the simulated NMSZ ruptures. The scenarios that in the simulations generate the largest ground motions in Memphis are uni-lateral ruptures from the north and bi-lateral ruptures on the southwest segment due to directivity, which can generate SAs up to 0.5 g and PGVs up to about 5 cm/s. Other scenarios show SAs and PGVs up to 0.1g and near 5 cm/s, respectively, in Memphis. These findings are emphasized in Figure 16, showing BB velocity seismograms predicted in Memphis for all nine scenarios, which also shows a duration of up to 30-40 s for the strongest shaking. St Louis and Evansville are located 150-200 km north of the northern extent of the NMSZ, and for most scenarios are exposed to minor peak motions (<0.05 g for SAs and PGAs, <2 cm/s). Exceptions, however, include bi-lateral and uni-lateral ruptures from the south on the southwest segment, where SAs and PGVs can reach 0.1g and 5 cm/s, respectively. The latter exception is particularly relevant for Evansville, which is located in the direction of rupture from this segment. Figure 17, showing BB velocity synthetics predicted in St Louis for all nine scenarios, illustrates these findings further.

Discussion and conclusions

We have simulated wave propagation for M_w7.4-7.7 earthquakes in the New Madrid Seismic Zone using a new 3D Community Velocity model of the Central United States. The largest peak ground motions are found on or immediately next to the fault traces. Out of the major urbanized areas in the region, Memphis experiences the largest long-period peak ground motions, while the values for St Louis, MO and Evansville, IN are much smaller. Combined with a duration of the shaking of up to 30-40 seconds, these worst-case scenarios could inflict sizable damage on the built environment, in particular in Memphis. M_w7.7 scenarios on the southwest segment with bi-lateral or north-south rupture direction tend to generate the largest ground motions (PGVs up to ~5 cm/s and SAs up to ~0.5g) in Memphis. Peak ground motions in St Louis and Evansville (<0.1g and PGVs below ~2 cm/s) will be felt, but likely not generate significant damage from

any of the NMSZ scenarios.

The resolution of the velocity model for the Central United States varies strongly within the area considered in this study. The heavily urbanized regions, in particular in and around Memphis and St Louis, MO, are generally well constrained. However, other parts of the model, where constraints from data are sparse, contain larger uncertainties. We obtained a generally good fit between simulation and recorded data for the 2008 M_w5.2 Mt Carmel, Illinois, earthquake. However, additional validation of the 3D velocity model of the Central United States should be carried out in future studies. Such validation studies should also aim to refine the relations for Q_p and Q_s.

Our ensemble of dynamic rupture models is based on a relatively small subset of possible parameterizations. For example, we selected a fractal model to generate the stochastic component of the initial stress distribution for all of the dynamic simulations. Mai and Beroza (2002) show that the fractal model describes the power spectrum of published slip distributions equally as well as von Karman and exponential autocorrelation functions, at least for faults with small aspect ratios. While there are many studies recommending self-similar, fractal or von Karman stress distributions based on the spectral behavior of slip (Guatteri et al., 2003; Mai and Beroza, 2002; Ripperger et al., 2007, Schmedes et al., 2010), we are not aware of any studies that recommend a specific distribution based directly on observed ground motions.

A further limitation is that all of our rupture models are based on a simple slip-weakening law, which has been used extensively in both numerical and observational studies (e.g., Andrews, 1976; Madariaga et al., 1998; Fukuyama et al., 2003; Cruz-Atienza et al., 2009). However, it is known that laboratory observations are better explained with a rate-and-state variable friction law (Scholz, 1998) which describes the dependency of the friction coefficient on slip velocity (i.e., ~velocity strengthening or velocity weakening). Many studies support the presence of a velocity strengthening layer near the surface (Day and Ely, 2002; Somerville and Pitarka, 2006; Dalguer and Mai, 2008; Kaneko et al., 2008). Because the slip-weakening friction model implemented in our dynamic rupture code does not model rate-and-state friction directly, we have emulated the velocity strengthening layer in the crust by adjusting μ_d and d_0 as described above.

Despite these limitations and uncertainties of the cusvm and ground motion estimates, our results indicate that the societal impact of M_w7.4-7.7 earthquakes in the NMSZ depends on the epicentral locations on the individual fault segments, primarily from directivity effects. Additional earthquake scenarios should be simulated in the future to more accurately assess the impact on man-made structures and population of the Central United States.

Acknowledgements

This work was supported through DOI U.S. Geological Survey # G10AP00007. The simulations were carried out on the Kraken parallel computer at NICS. The 3D velocity

model was developed by Leonardo Ramirez-Guzman, of the USGS, Golden Colorado (now at UNAM, Mexico). This work was carried out as part of a working group collaboration between USGS Golden and Memphis, URS, SDSU, and CERI.

References

Anderson, J.G., P. Bodin, J.N. Brune, J. Prince, S.K. Singh, R. Quaas, and M. Onate (1986). Strong ground motion from the Michoacan, Mexico, earthquake, Science 233, 1043-1049.

Andrews, D.J. (1976). Rupture propagation with finite stress in antiplane strain, Jour. Geopys. Res. 81, 3575-3582.

Bakun, W.H. and M.G. Hopper (2004). Magnitudes and locations of the 1811-1812 New Madrid, Missouri, and the 1886 Charleston, South Carolina, earthquakes, *Bull. Seis. Soc. Am*. **94**, 64-75.

Borcherdt, R.D. (1994). Estimates of site-dependent response spectra for design (methodology and justification), Earthquake Spectra 10, 617-653.

Brocher, T.M. (2005). Empirical relations between elastic wavespeeds and density in the earth's crust, *Bull. Seis. Soc. Am*. **95**, 2081-2092.

Cerjan, C., Kosloff, D., Kosloff, R, Reshef, M. (1985) Absorbing boundary conditions for acoustic and elastic wave equations, *Bull. Seis. Soc. Am.* **67**, 1529-1540.

Campbell, K.W., and Y. Bozorgnia (2008). NGA ground motion model for the geometric mean horizontal component of PGA, PGV, PGD and 5%-damped PSA at spectral periods between 0.01 and 10 s, Earthquake Spectra 24, 99-138.

Cruz-Atienza, V.M., K.B. Olsen, and L.A. Dalguer (2009). Estimation of the breakdown slip from strong-motion seismograms: insights from numerical experiments, Bull. Seis. Soc. Am., 99, 3454-3469.

Cui, Y., K.B. Olsen, L. Lee, J. Zhou, P. Small, D. Roten, G. Ely, D.K. Panda, A. Chourasia, J. Levesque, S.M. Day, and P. Maechling (2010) Scalable earthquake simulation on petascale supercomputers, Proceedings of SC10, Nov 13-19, New Orleans, LA.

Dalguer, L.A. and S.M. Day (2007). Staggered-grid split node method for spontaneous rupture simulation, Jour. Geophys. Res. 112, B02302.

Dalguer, L.A., H. Miyake, S.M. Day, and K. Irikura (2008). Surface rupturing and buried dynamic-rupture models calibrated with statistical observations of past earthquakes, Bull. Seis. Soc. Am. 98, 1147.

Dalguer, L.A. and P.M. Mai (2008). Implications of style-of-faulting and loading characteristic on the dynamic rupture process, AGU Fall Meeting Abstract, 2008, D1798.

Day, S.M. and Bradley, C.R. (2001). Memory-efficient simulation of anelastic wave propagation, *Bull. Seism. Soc. Am.* **91**, 520-531.

Day, S.M. and G.P. Ely (2002). Effect of a shallow weak zone on fault rupture: numerical simulation of scale-model experiments, Bull. Seis. Soc. Am. 92, 3006-3021.

Dreger, D., E. Tinti, and A. Cirella (2007). Slip velocity function parameterization for broadband ground motion simulation, Seism. Soc. Am. 2007 Annual Meeting, Waikoloa, HI.

Fukuyama, E., T. Mikumo, and K.B. Olsen (2003). Estimation of the critical slip-weakening distance: theorerical background, Bull. Seis. Soc. Am. 93, 1835-1840.

Ginzburg, A., W. D. Mooney, A. W. Walter, W. J. Lutter, and H. H. Healy (1983). Deep structure of northern Mississippi Embayment, *Am. Assoc. Pet. Geol. Bull.* **67,** 2031–2046.

Graves, R.W., and A. Pitarka (2010). Broadband ground-motion simulation using a hybrid approach, Bull. Seis. Soc. Am. 100, 5A, 2095-2123.

Guatteri, M., P.M. Mai, and G.C. Beroza (2004). A pseudo-dynamic approximation to dynamic rupture models for strong ground motion prediction, *Bull. Seis. Soc. Am*., Vol 94 (6), pp. 2051-2063.

Guatteri, M., P.M. Mai, G.C. Beroza, and J. Boatwright (2003). Strong ground-motion prediction from stochastic-dynamic source models (2003), Bull. Seis. Soc. Am. 93, 301-313.

Hartzell, S., M. Guatteri, P.M. Mai, P.C. Liu, and M. Fisk (2005). Calculation of broadband time histories of ground motion, part II: kinematic and dynamic modeling using theoretical Green's functions and comparison with the 1994 Northridge earthquake, Bull. Seis. Soc. Am. 95, 614-645.

Hartzell, S. and C. Mendoza (2011). Source and site response study of the 2008 Mount Carmel, Illinois, earthquake. Bull Seis. Soc. Am. 101, 951-963.

Hough, S.E., P.A. Friberg, R. Busby, E.F. Field, and K.H. Jacob (1990). Did mud cause freeway collapse? *EOS* Trans. Am. Geophys. Un. **70**, 1497-1504.

Hough, S.E. J. G. Armbruster, L. Seeber, and J. F. Hough (2000). On the modified Mercalli intensities and magnitudes of the 1811–1812 New Madrid earthquakes, *J. Geophys. Res.* **105,** 23,839–23,864.

Irikura, K. and K. Kamae (1994). Estimation of strong ground motion in broad-frequency band based on a seismic source scaling model and an empirical Green's Function Technique, Annals of Geophysics 37, No 6.

Johnston, A. C., and E. S. Schweig (1996). The enigma of the New Madrid earthquakes of 1811–1812, *Ann. Rev. Earth Planet. Sci.* **24,** 339–384.

Kaneko, Y., N. Lapusta, and J.P. Ampuero (2008). Spectral element modeling of spontaneous rupture on rate and state faults: effect of velocity strengthening friction at shallow depths, Jour. Geophys. Res 113, B9, B09317.

Macpherson, K. A., E. W. Woolery, Z. Wang, and P. Liu (2010). Three-dimensional Long-period Ground-motion Simulations in the Upper Mississippi Embayment, *Seism. Res. Lett*., 81, 391-405, doi: 10.1785/gssrl.81.2.391.

Madariaga, R., K.B. Olsen, and R.J. Archuleta (1998). Modeling dynamic rupture in a 3D earthquake fault model, Bull. Seis. Soc. Am. 88, 1182-1197.

Mai, P.M. and G.C. Beroza (2002). A spatial random field model to characterize complexity in earthquake slip, Jour. Geophys. Res (Solid Earth), 107 (Nov), 2308.

Mai, P.M. and G.C. Beroza (2003). A hybrid method for calculating near-source, broadband seismograms: applications to strong motion prediction, Phys. Earth. Planet Int. 137, 183-199.

Mai, P.M., W. Imperatori, and K.B. Olsen (2010). Hybrid broadband ground motion simulations: combining long-period deterministic synthetics with high-frequency multiple S-to-S backscattering, Bull. Seis. Soc. Am., 100, 5A, 2124-2142.

Mena, B., P.M. Mai, K.B. Olsen, M.D. Purvance, and J.N. Brune (2010). Hybrid broadband ground-motion simulation using scattering Green's functions: application to large-magnitude events, Bull. Seis. Soc. Am. 100, 5A, 2143-2162.

Mooney, W. D., M. C. Andrew, A. Ginzburg, D. A. Peters, and R. A. Hamilton (1983). Crustal structure of the northern Mississippi embayment and a comparison with other continental rift zones, *Tectonophysics* **94,** 327–348.

Olsen KB (1994) Simulation of three-dimensional wave propagation in the Salt Lake Basin, *Ph.D. Thesis*, University of Utah, Salt Lake City, Utah, 157 p.

Olsen KB, Day SM, Bradley CR (2003) Estimation of Q for long-period (>2 s) waves in the Los Angeles Basin, *Bull. Seis. Soc. Am*. **93**, 627-638.

Olsen KB, Day SM, Minster JB, Cui Y, Chourasia A, Faerman M, Moore R, Maechling P, Jordan T (2006) Strong shaking in Los Angeles expected from southern San Andreas earthquake, *GRL* **33**, L07305, doi:10.1029/2005GL025472.

Olsen KB, Day SM, Minster JB, Cui Y, Chourasia A, Okaya D, Maechling P, Jordan T (2008) TeraShake 2: simulation of Mw 7.7 earthquakes on the southern San Andreas fault with spontaneous rupture description, *Bull. Seis. Soc. Am,* 98, 1162-1185.

Ramirez-Guzman, L., O.S. Boyd, S. Hartzell, and R.A. Williams (2012). Seismic velocity model of the central United States (Version 1): description and simulation of the 18 April 2008 Mt Carmel, Illinois earthquake, Bull. Seis. Soc. Am., under revision.

Schmedes, J., R.J. Archuleta, and D. Lavallee (2010). Correlation of earthquake source parameters inferred from dynamic rupture simulations, Jour. Geophys. Res. 115.

Scholz, C.H. (1998). Earthquakes and friction laws, Nature 391, 6662, 37-42.

Singh, S.K., E. Mena, and R. Castro (1988). Some aspects of source characteristics of the 19 September 1985 Michoacan earthquake and ground motion amplification in and near Mexico City from strong motion data, *Bull. Seis. Soc. Am.* **78**, 451-477.

Somerville, P.G. and A. Pitarka (2006). Differences in earthquake source and ground motion characteristics between surface and buried earthquakes, Procs. of the 8th National Conference on Earthquake Engineering.

Somerville, P.G., R.W. Graves, N.F. Collins, S.G. Song, S. Ni and P. Cummins (2009). Source and ground motion models of Australian earthquakes. Proceedings of the 2009 Annual Conference of the Australian Earthquake Engineering Society, Newcastle, December 11-13.

Tuttle, M.P., E.S. Schweig, J.D. Sims, R.H. Lafferty, L.W. Wolf, and M.L. Haynes (2002). The earthquake potential of the New Madrid seismic zone, *Bull. Seis. Soc. Am.* **92**, 2090-2089.

U.S. Geological Survey Staff (1990). The Loma Prieta, California, earthquake: An anticipated event, *Science* **247**, 286-293

Wells, D.L. and K.J. Coppersmith (1994). New empirical relationships among magnitude, rupture length, rupture width, rupture area, and surface displacement, Bull. Seis. Soc. Am. 84, 974-1002.

Zeng, Y.H., F. Su, and K. Aki (1991). Scattering wave energy propagation in a random isotropic scattering medium. 1. Theory, Jour. Geophys. Res. 96, 607-619.

Zeng, Y.H., K. Aki, and T.L. Teng (1993). Mapping of the high-frequency source radiation for the Loma-Prieta earthquake, California, Jour. Geophys. Res. 98, 11981-11993.

Zeng, Y.H., J.G. Anderson, and S. Feng (1995). Subevent rake and random scattering effects in realistic ground motion simulations, Geophys. Res. Lett. 22, 17-20.

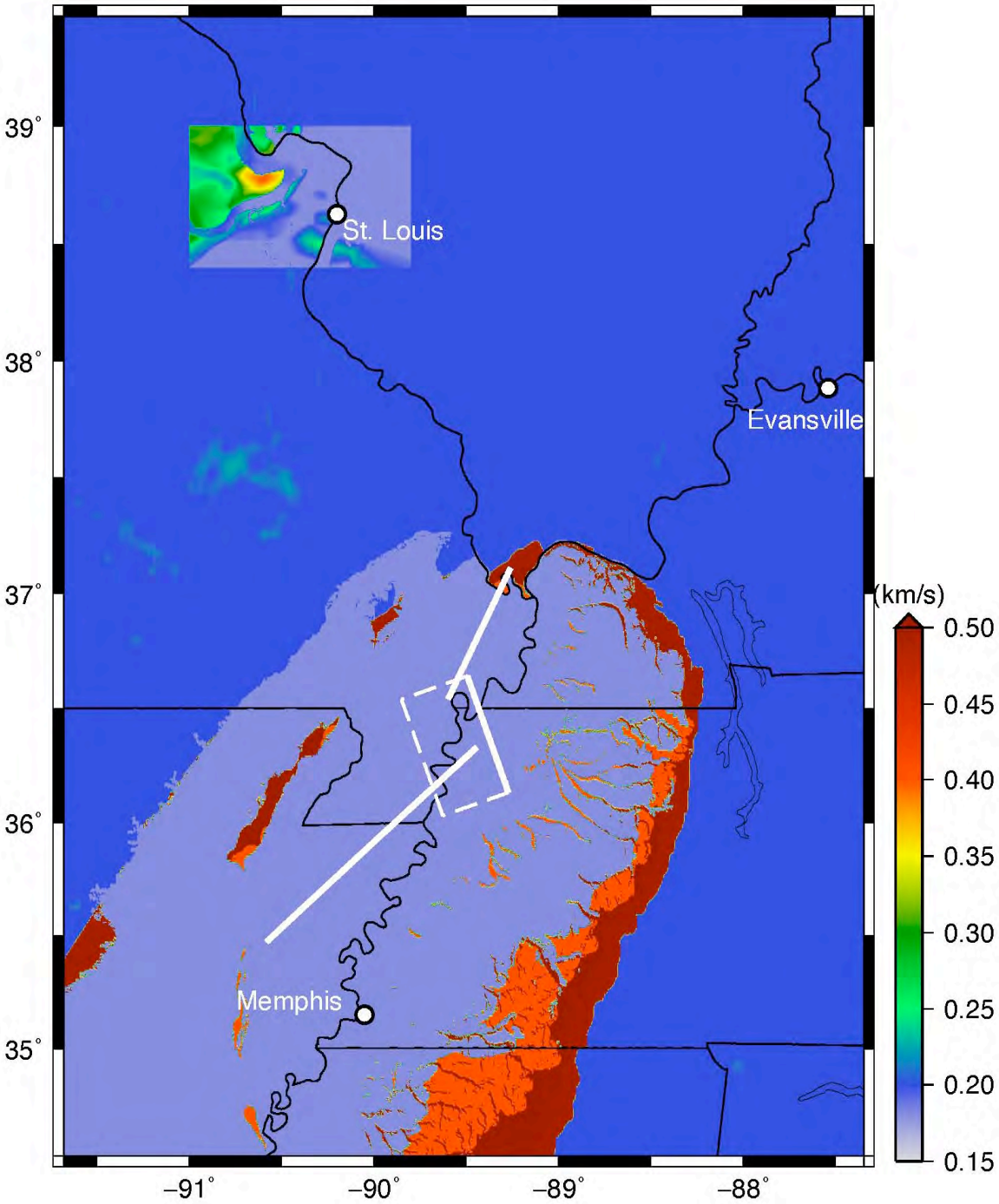

Figure 1. Surface slice of S-wave velocities from the Central US CVM used in the simulations. The white lines depict the surface projections of the three fault segments used for simulating ground motions in the Central US.

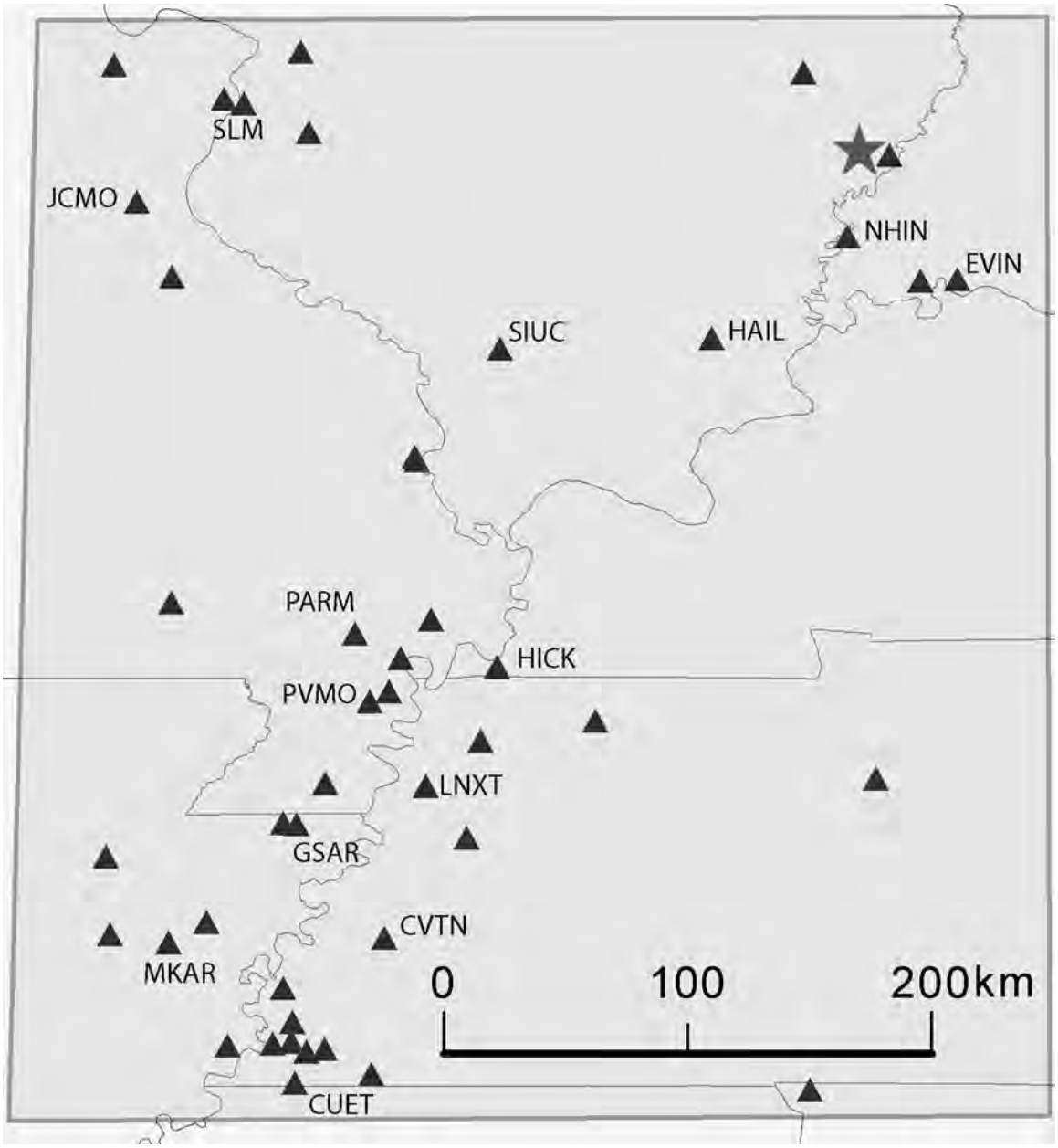

Figure 2. Location map. Triangles depict locations of stations used for the comparison of data and simulation in Figure 2. The star depicts the epicenter of the 2008 Mt Carmel, IL, earthquake.

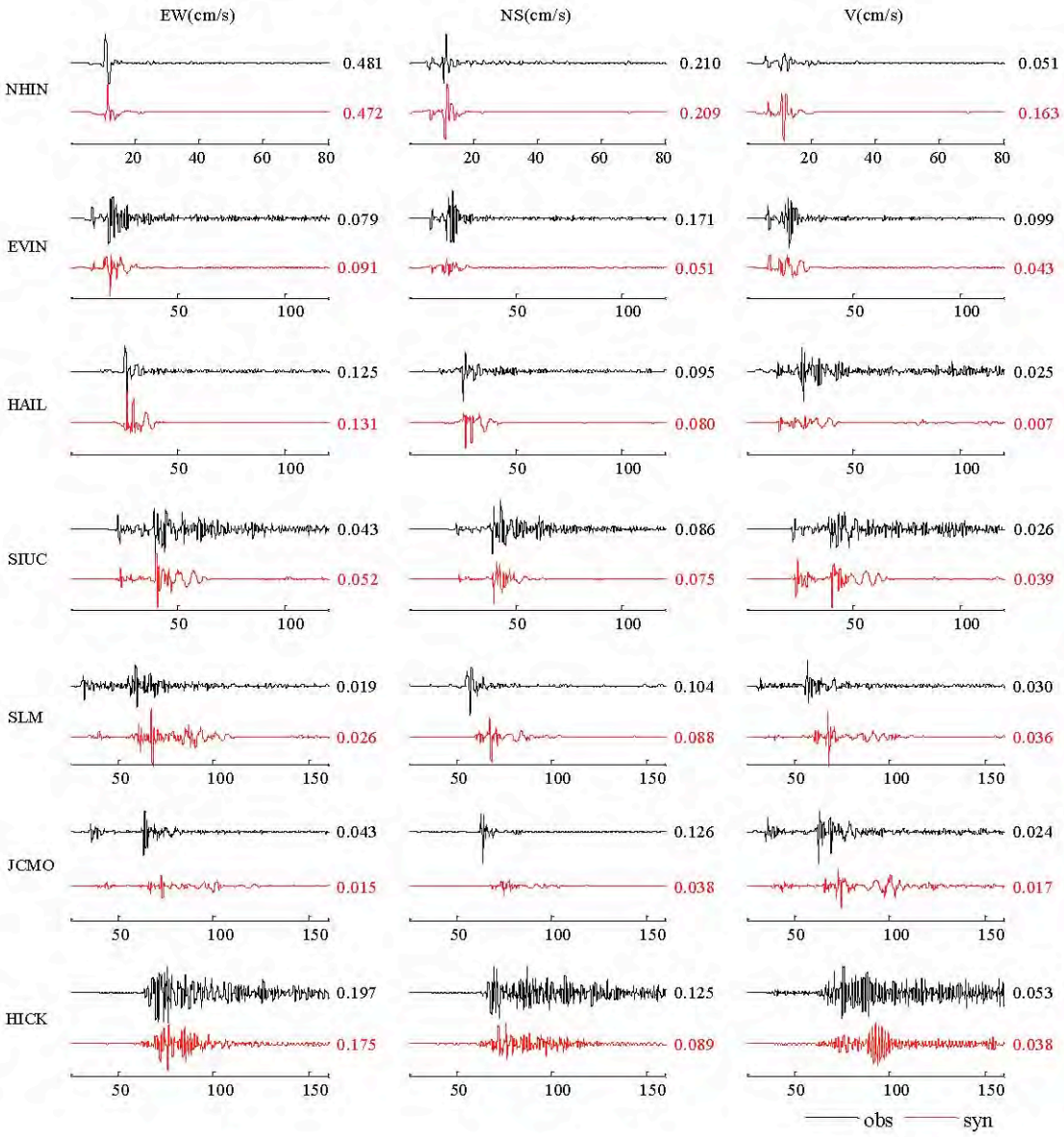
EW(cm/s)
NS(cm/s)
V(cm/s)
NHIN
0.481
0.472
0.210
0.209
0.051
0.163
EVIN
0.079
0.091
0.171
0.051
0.099
0.043
HAIL
0.125
0.131
0.095
0.080
0.025
0.007
SIUC
0.043
0.052
0.086
0.075
0.026
0.039
SLM
0.019
0.026
0.104
0.088
0.030
0.036
JCMO
0.043
0.015
0.126
0.038
0.024
0.017
HICK
0.197
0.175
0.125
0.089
0.053
0.038
obs
syn

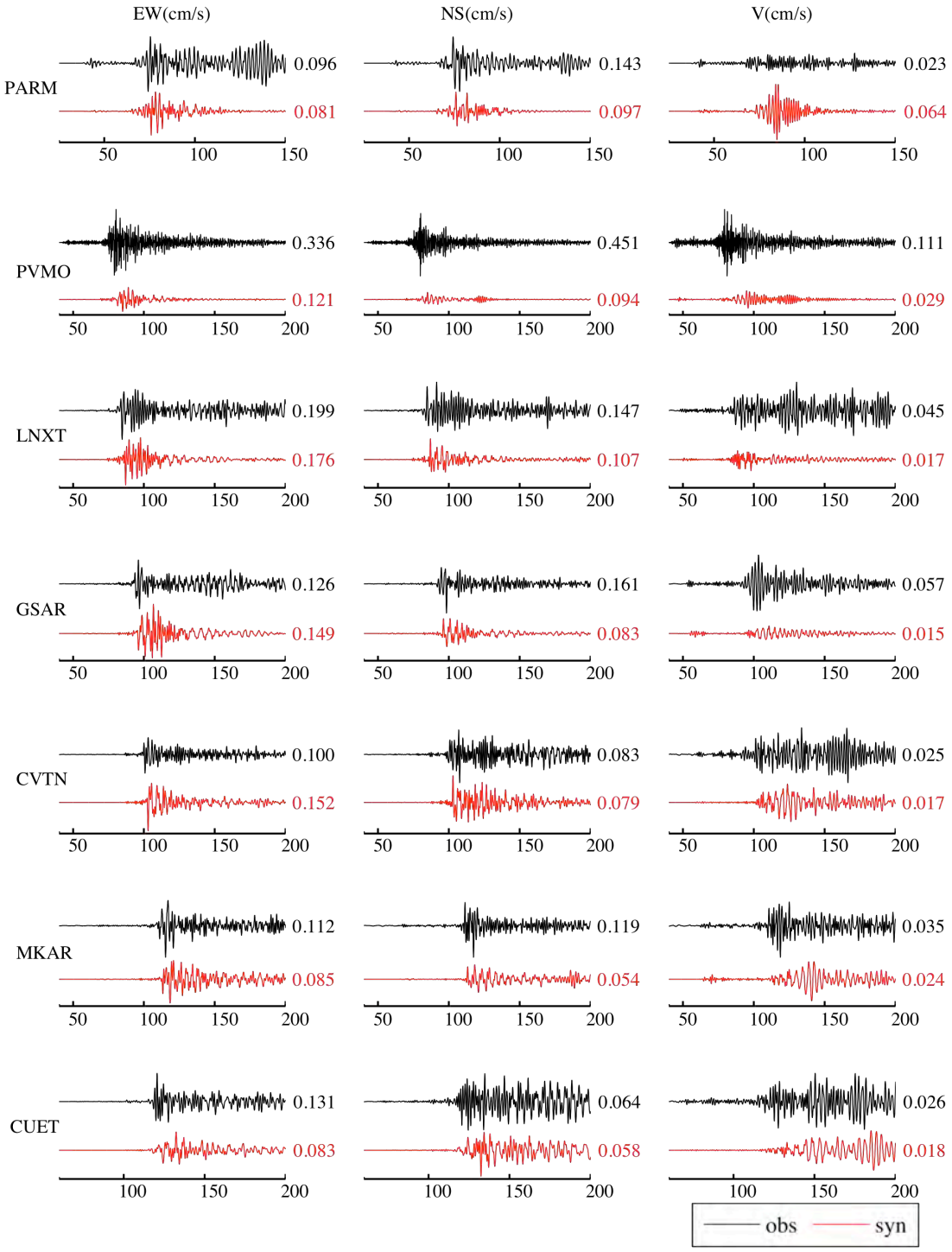

Figure 3. Comparison of 0-1Hz synthetics to data recorded at stations shown in Figure 2 for the 2008 Mt Carmel earthquake.

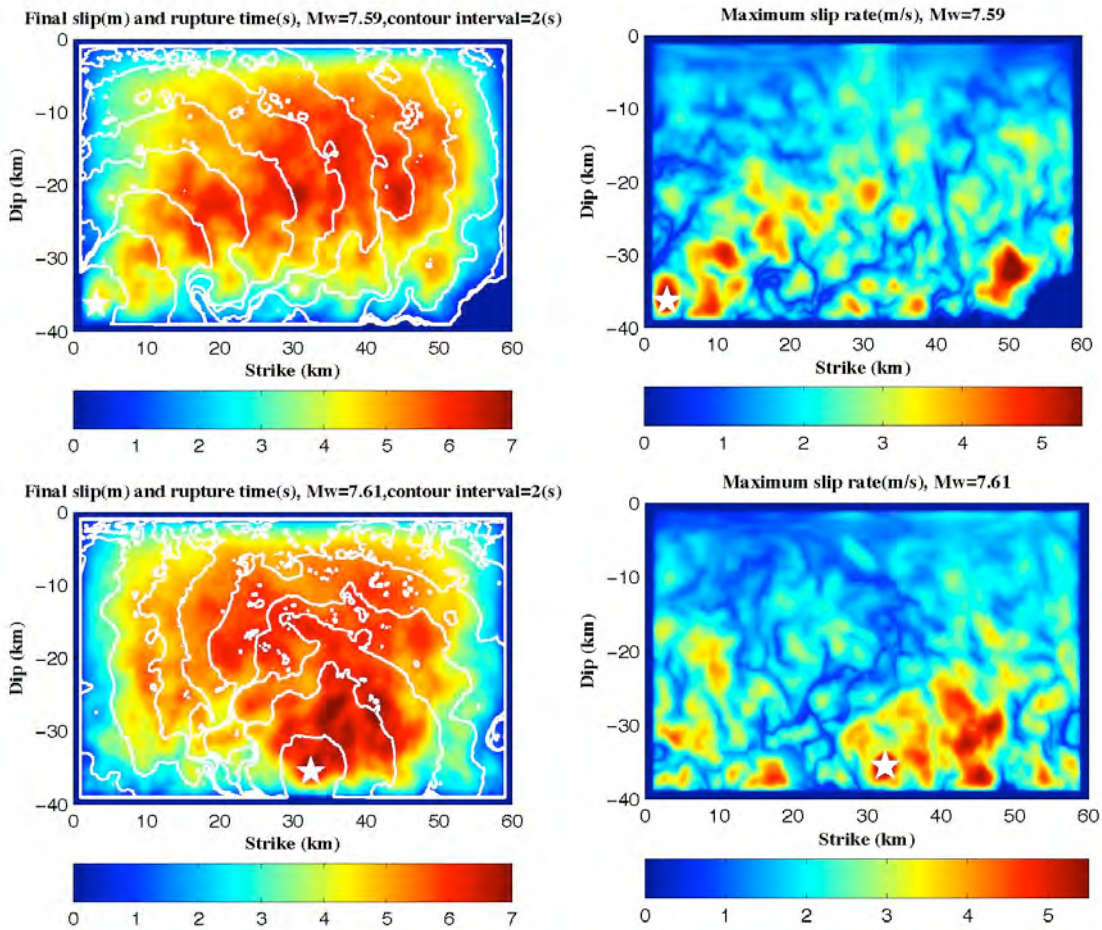

Figure 4. Dynamic rupture models for the central Segment used in the Central US ground motion simulations. (top) Uni-lateral and (bottom) bi-lateral rupture. (left) slip and (right) maximum slip rate on the fault. The source for the uni-lateral rupture was laterally mirrored to generate sources at both ends of the fault. Contours depict rupture time with an interval of 2s. The star depicts the hypocenter.

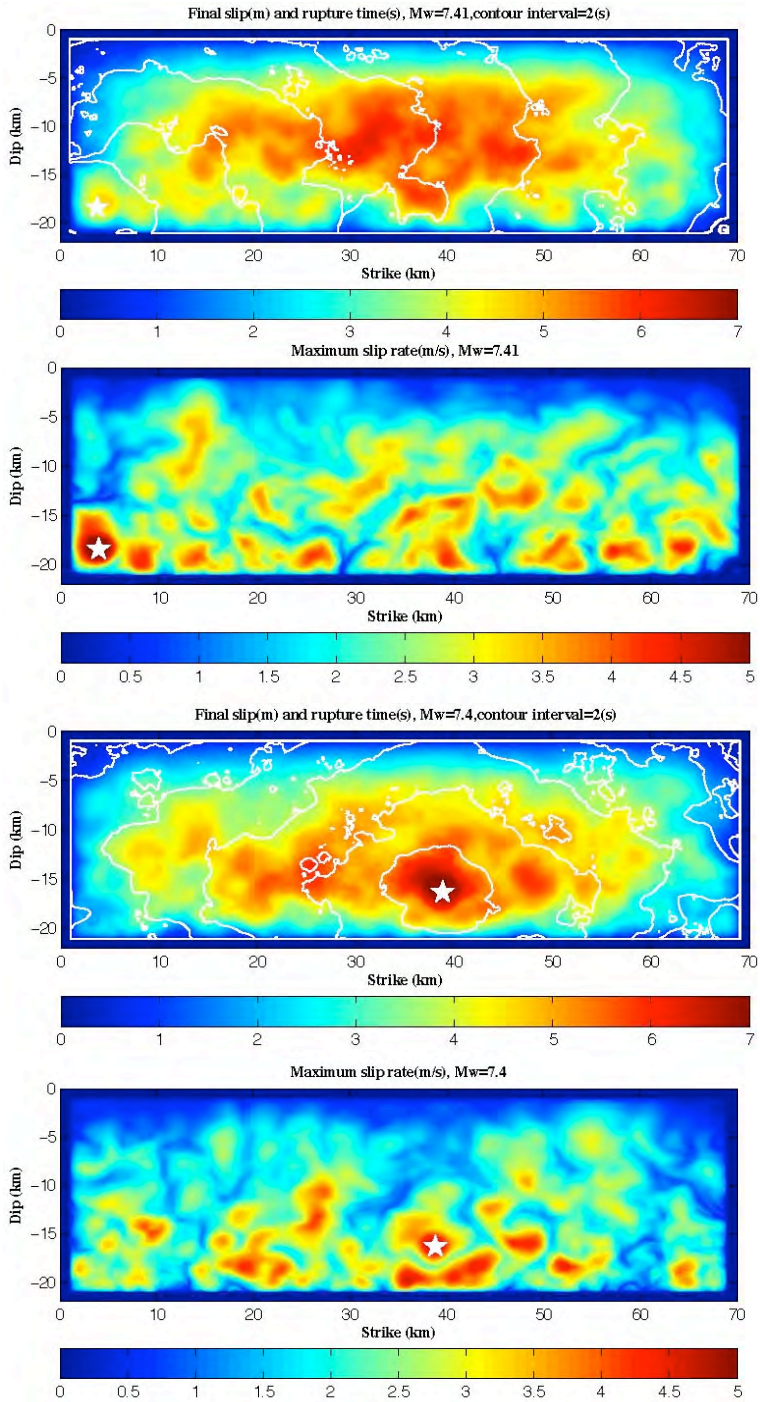

Figure 5. Dynamic rupture models for the NE segment used in the Central US ground motion simulations. From top to bottom: slip distribution for uni-lateral rupture, maximum sliprate for uni-lateral rupture, slip distribution for bi-lateral rupture, and maximum sliprate for bi-lateral rupture. The source for the uni-lateral rupture was laterally mirrored to generate sources at both ends of the fault. Contours depict rupture time with an interval of 2s. The star depicts the hypocenter.

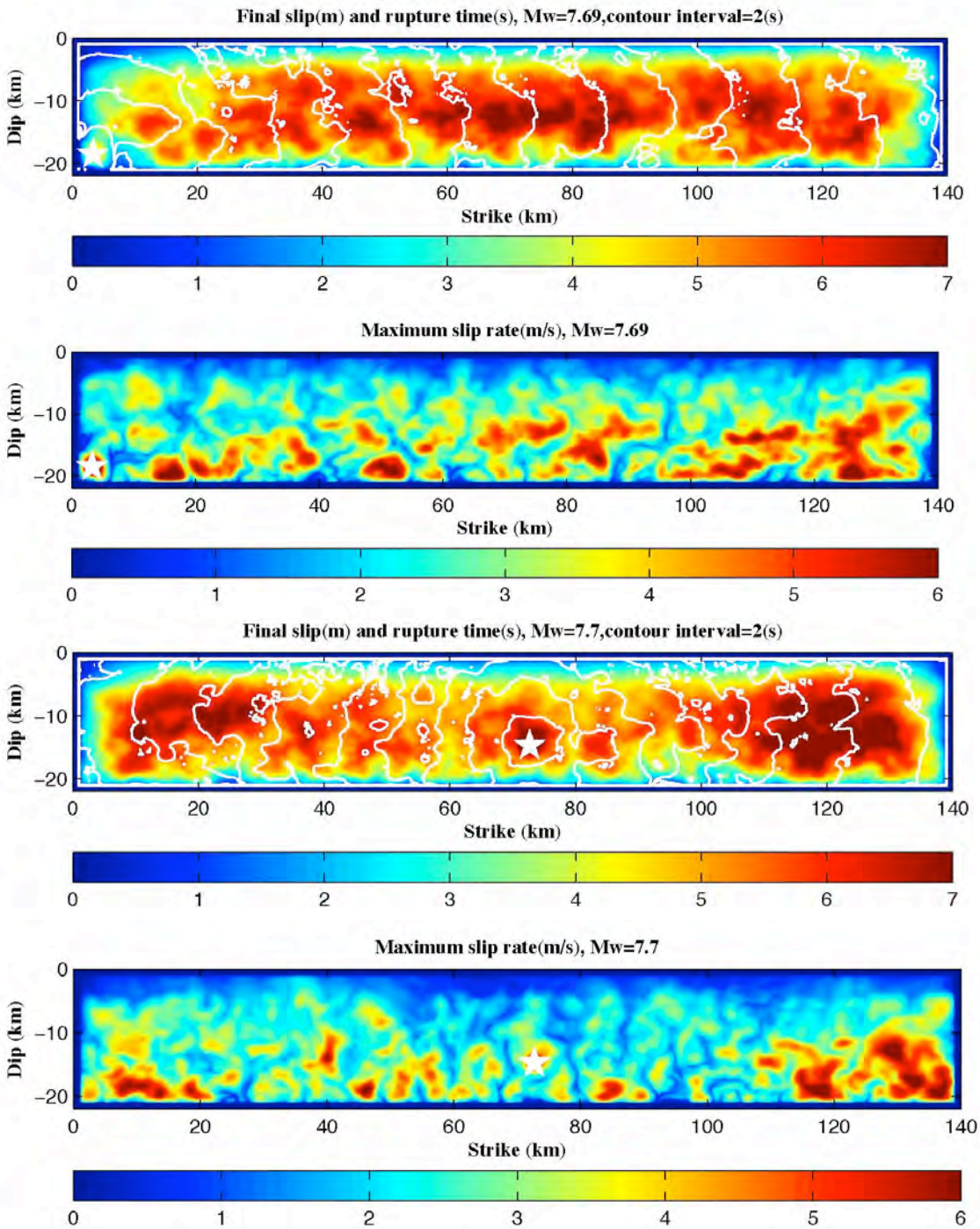

Figure 6. Same as Figure 5, but for the SW segment.

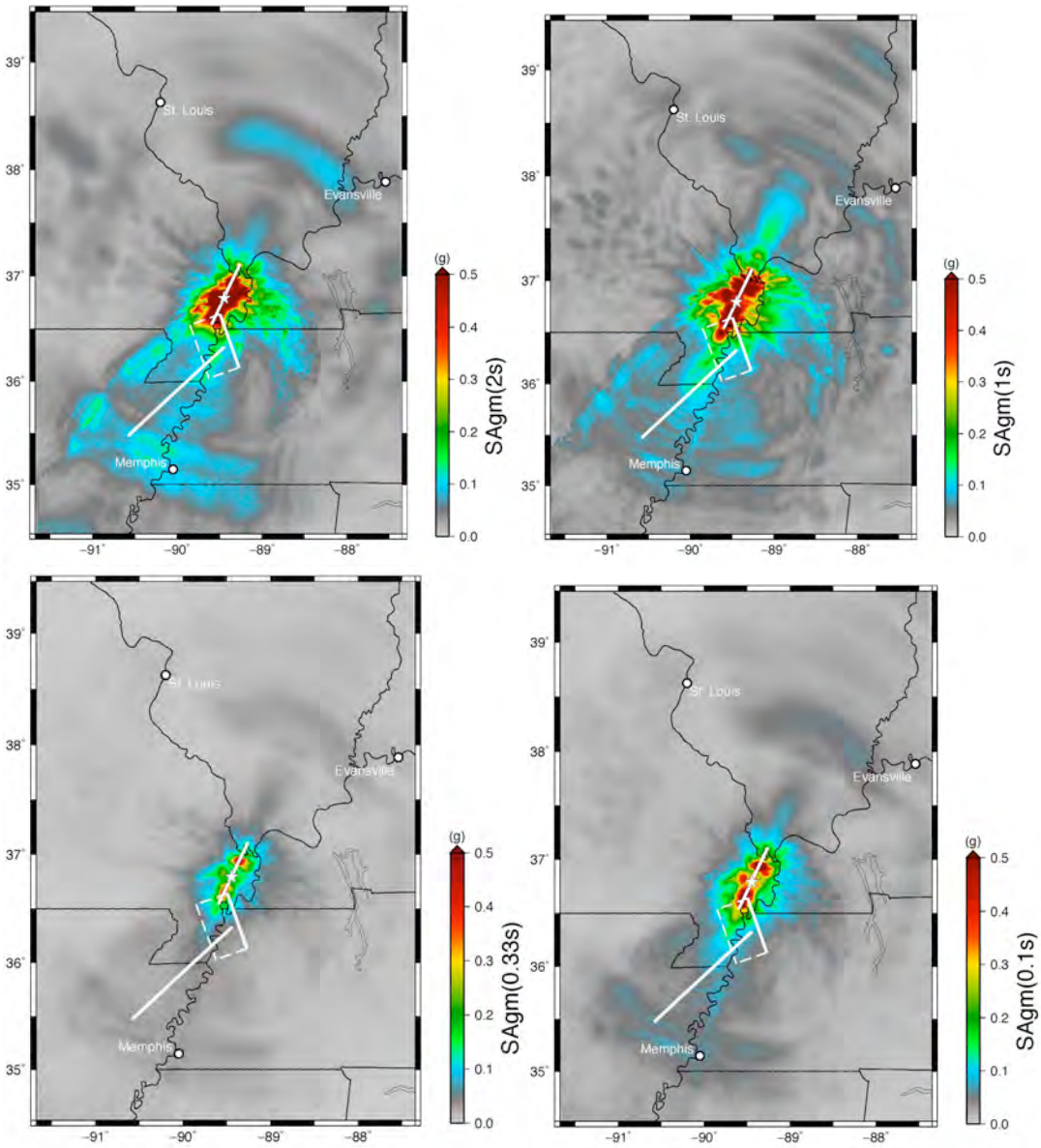
St. Louis
Evansville
Memphis
39°
38°
37°
36°
35°
−91°
−90°
−89°
−88°
(g)
0.5
0.4
0.3
0.2
0.1
0.0
SAgm(2s)
SAgm(1s)
SAgm(0.33s)
SAgm(0.1s)

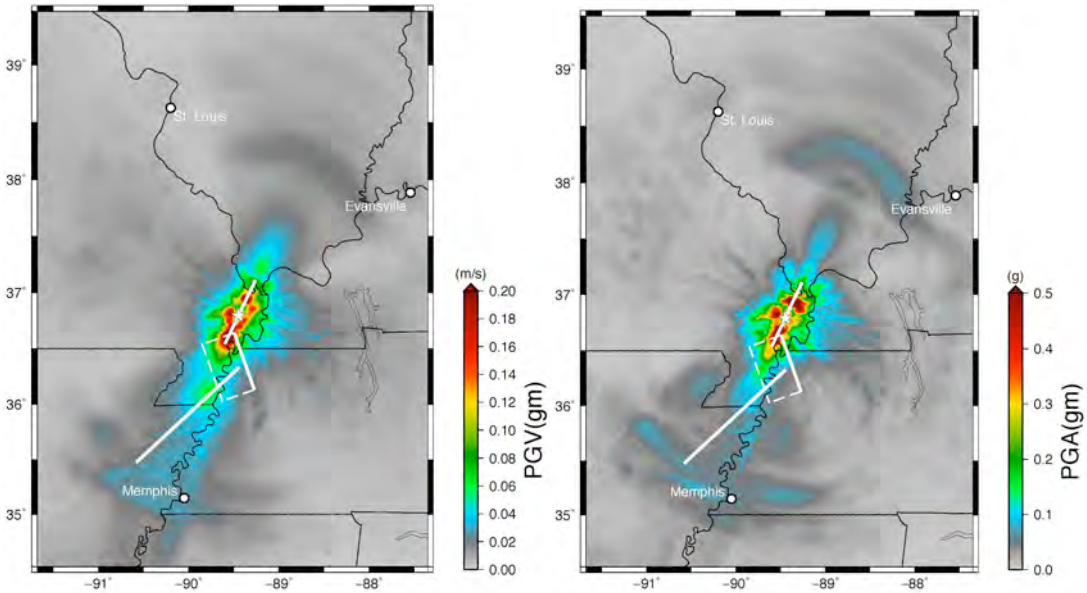

Figure 7. Ground motions (SA-2s, SA-1s, SA-0.33s, SA-0.1s, PGV, and PGA) for simulation of a M_w7.4 earthquake on the NE segment with bi-lateral rupture. The star depicts the epicenter, and the white lines depict the three fault segments.

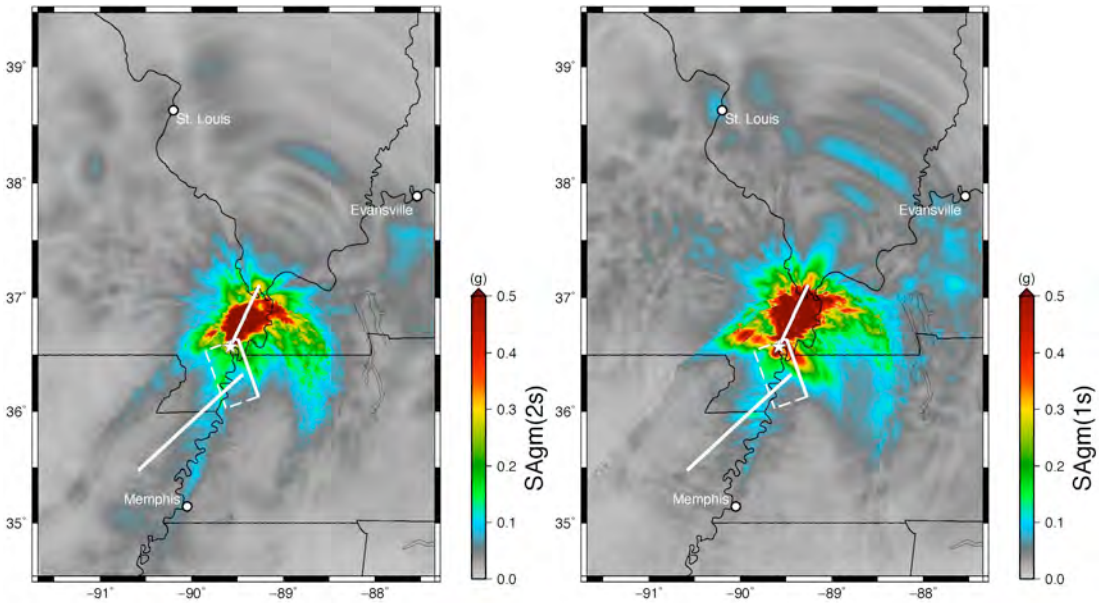

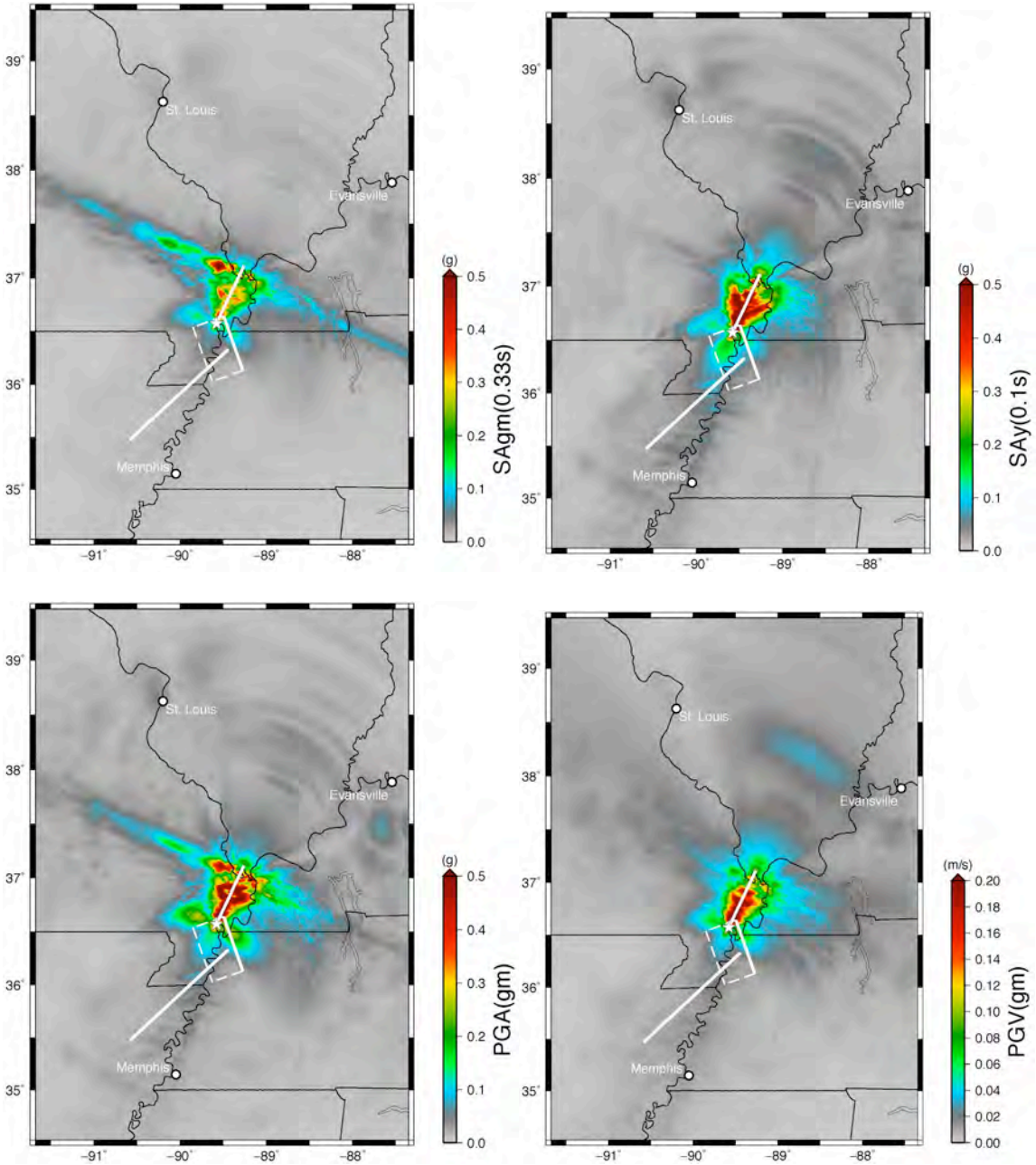

Figure 8. Same as Figure 7, but for a bi-lateral rupture from SW.

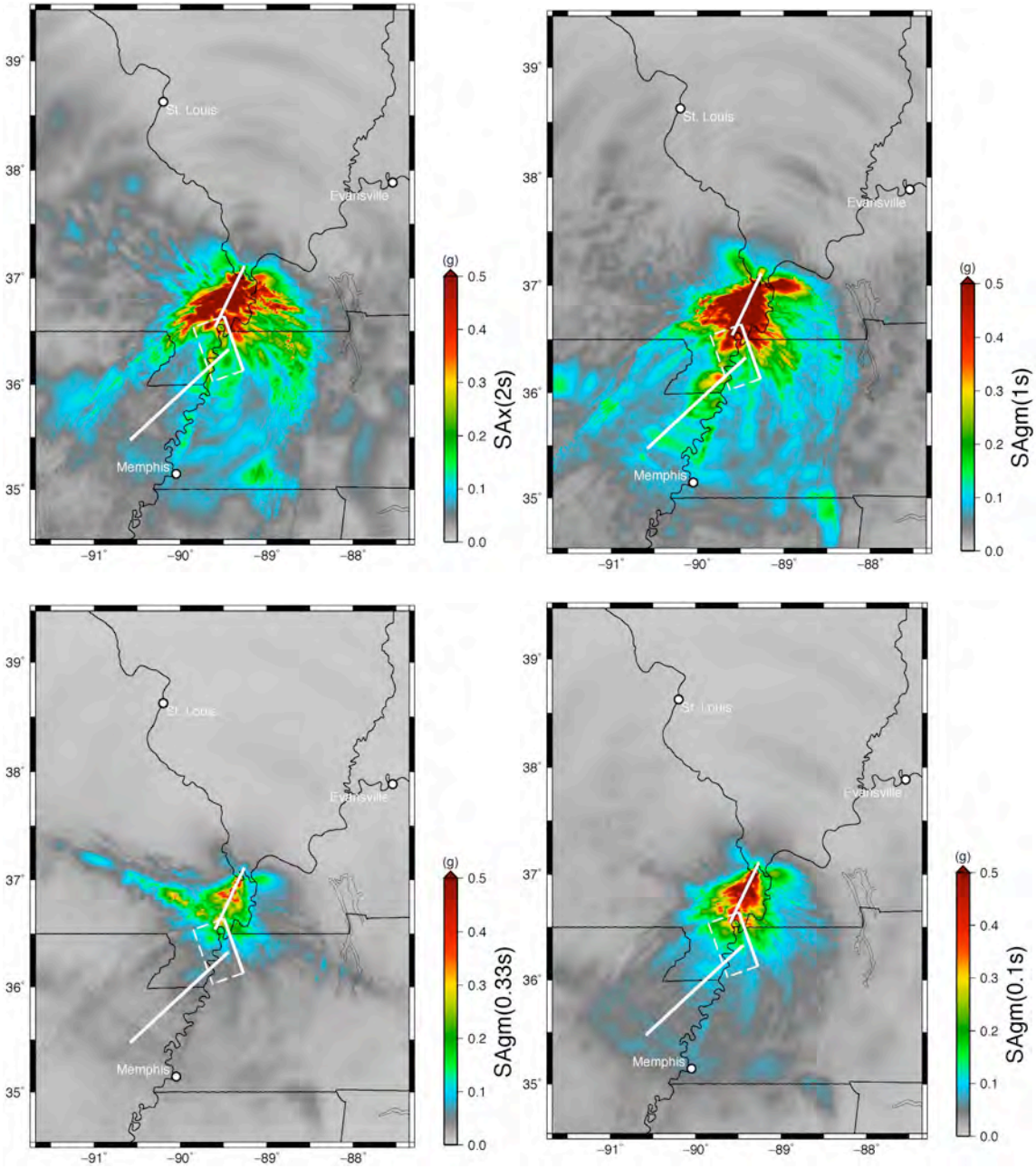
St. Louis
Evansville
Memphis
39°
38°
37°
36°
35°
−91°
−90°
−89°
−88°
(g)
0.5
0.4
0.3
0.2
0.1
0.0
SAx(2s)
SAgm(1s)
SAgm(0.33s)
SAgm(0.1s)

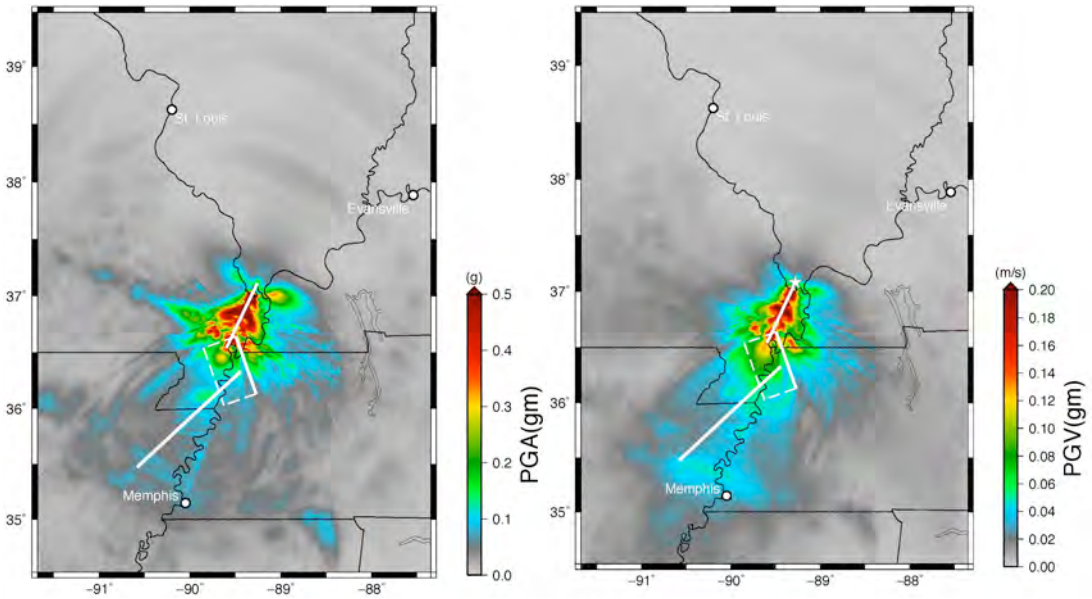

Figure 9. Same as Figure 7, but for a uni-lateral rupture from NE.

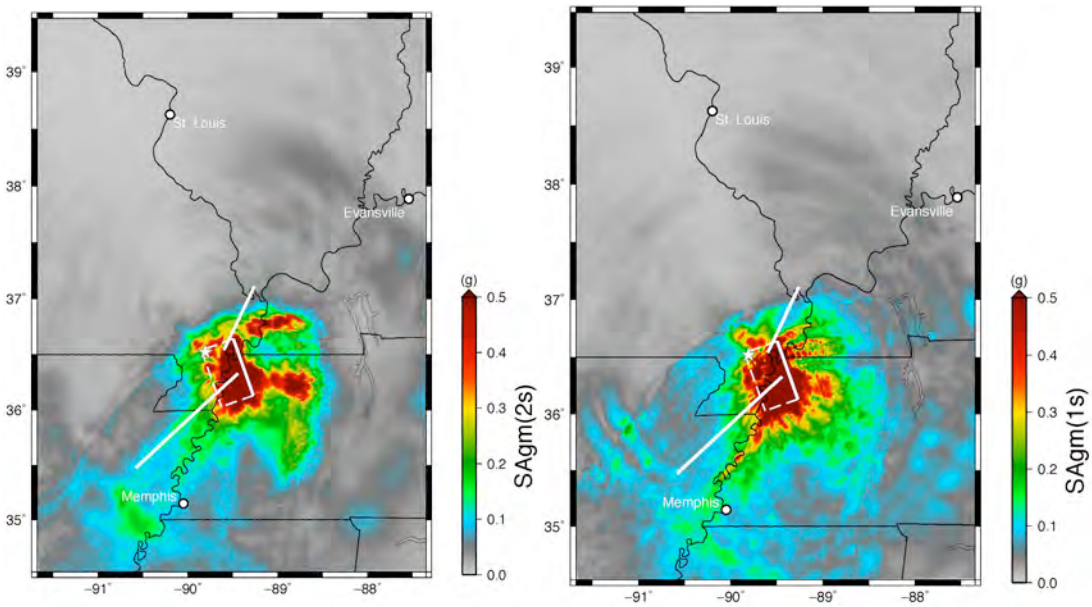

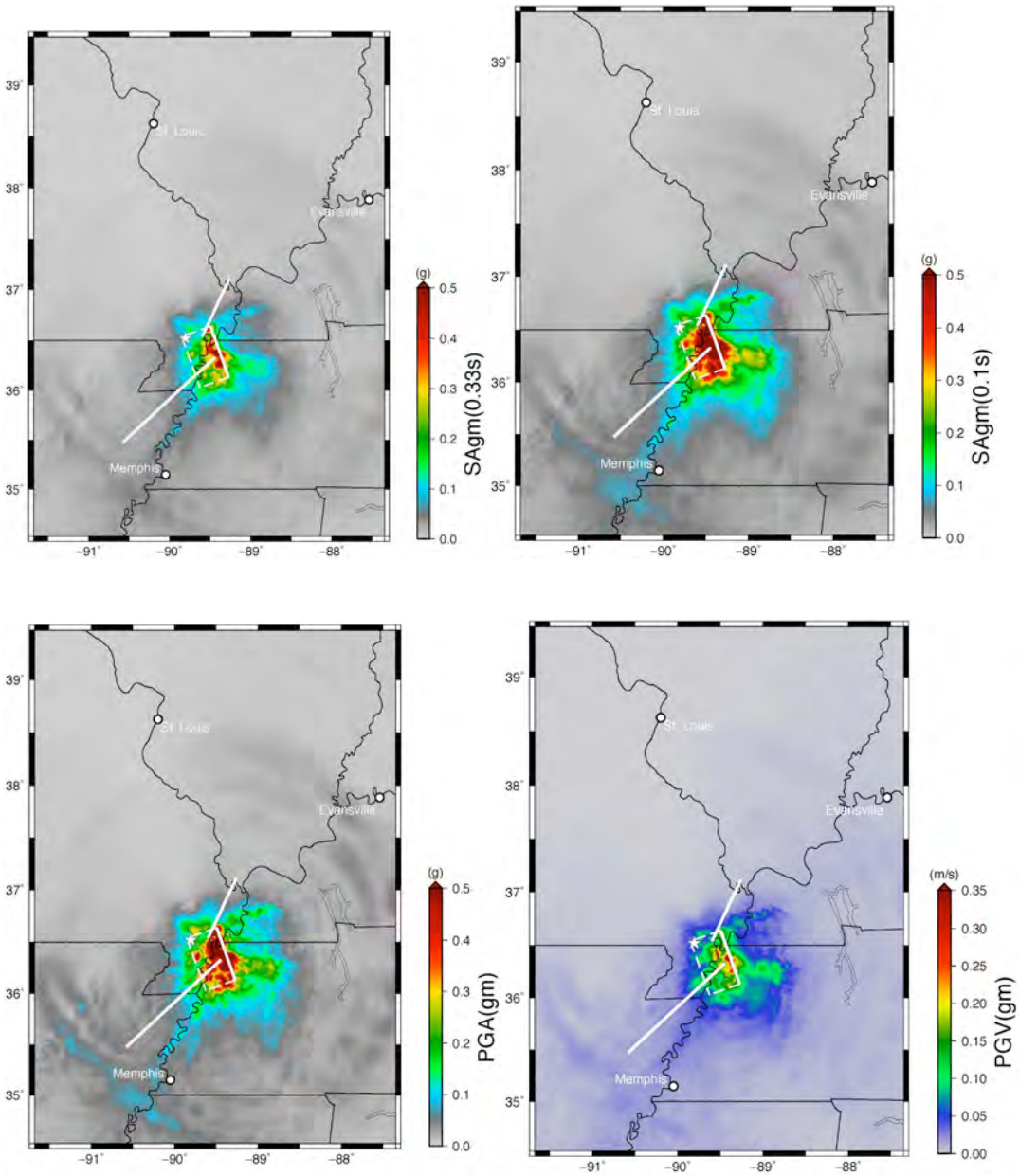

Figure 10. Same as Figure 7, but for a rupture on the central segment with hypocenter toward the NW.

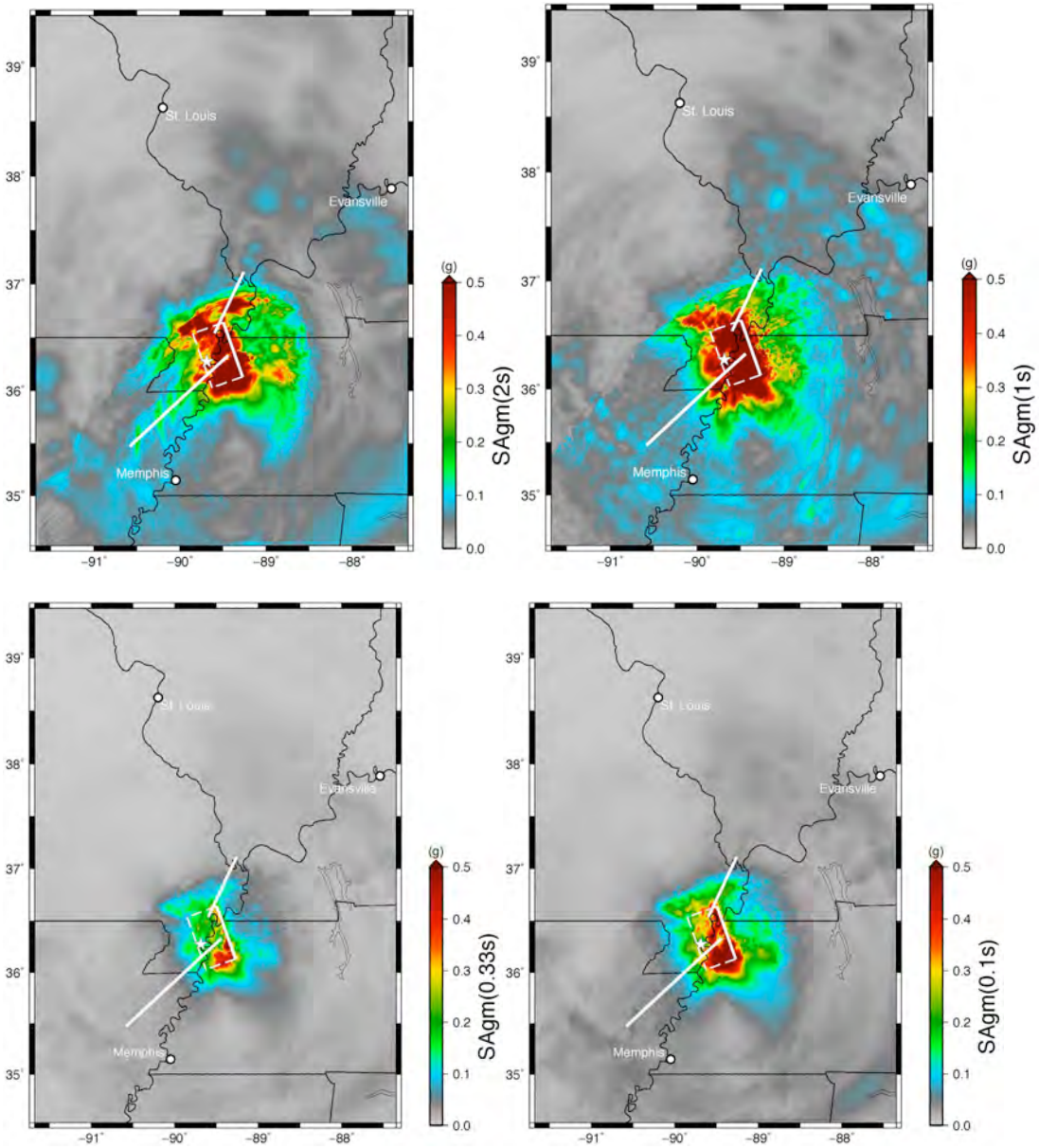
St. Louis
Evansville
Memphis
39°
38°
37°
36°
35°
−91°
−90°
−89°
−88°
(g)
0.5
0.4
0.3
0.2
0.1
0.0
SAgm(2s)
SAgm(1s)
SAgm(0.33s)
SAgm(0.1s)

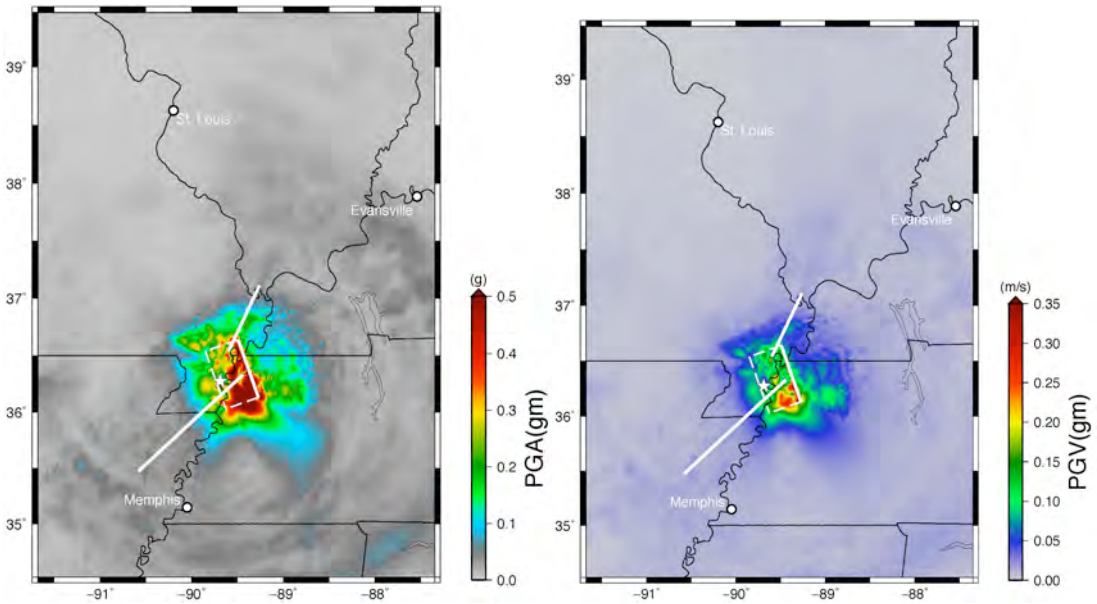

Figure 11. Same as Figure 10, but for a hypocenter toward the center bottom of the fault.

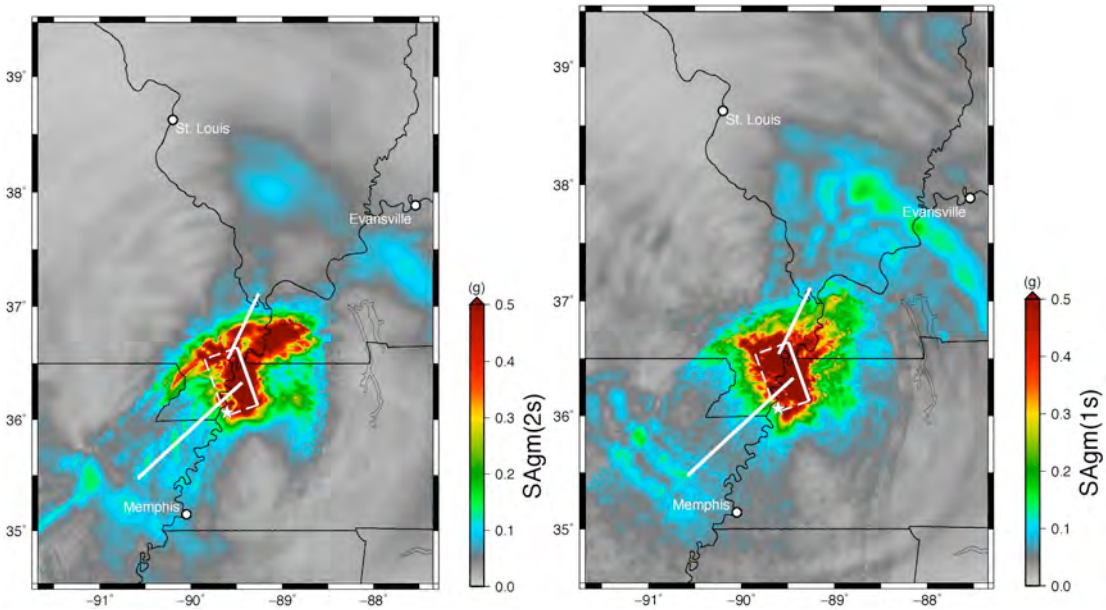

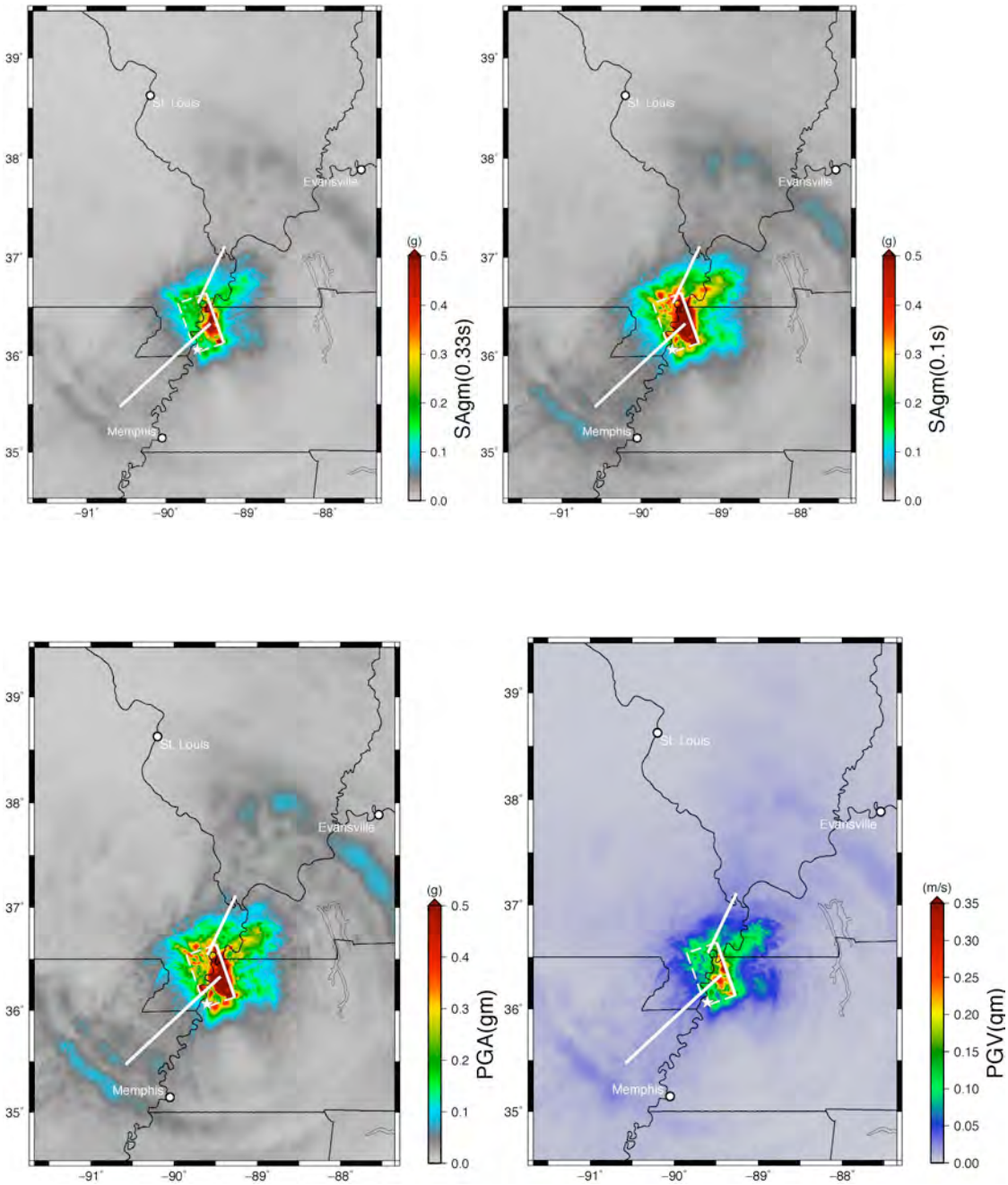

Figure 12. Same as Figure 10, but for a hypocenter toward the SE of the fault.

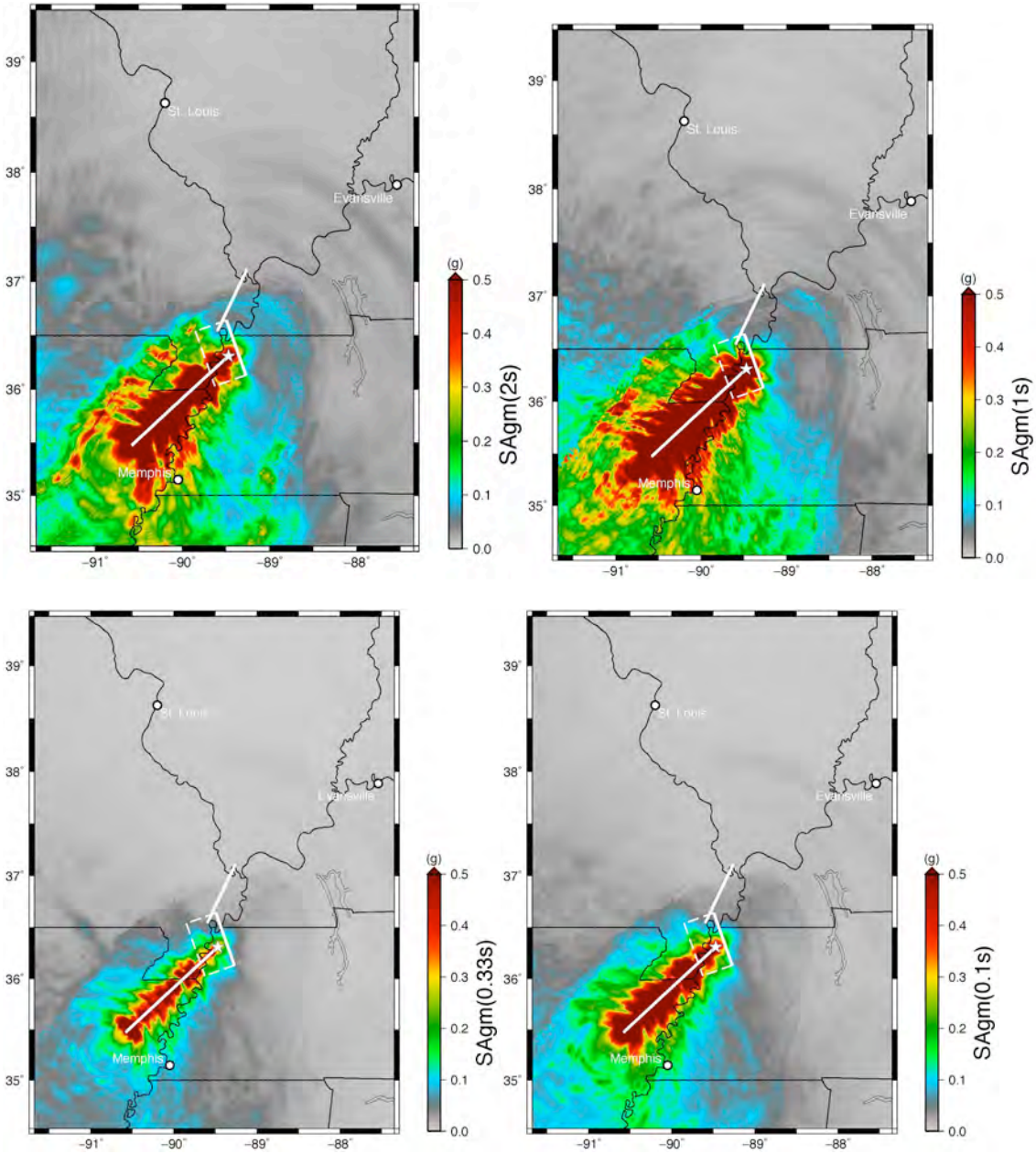
St. Louis
Evansville
Memphis
39°
38°
37°
36°
35°
−91°
−90°
−89°
−88°
(g)
0.5
0.4
0.3
0.2
0.1
0.0
SAgm(2s)
SAgm(1s)
SAgm(0.33s)
SAgm(0.1s)

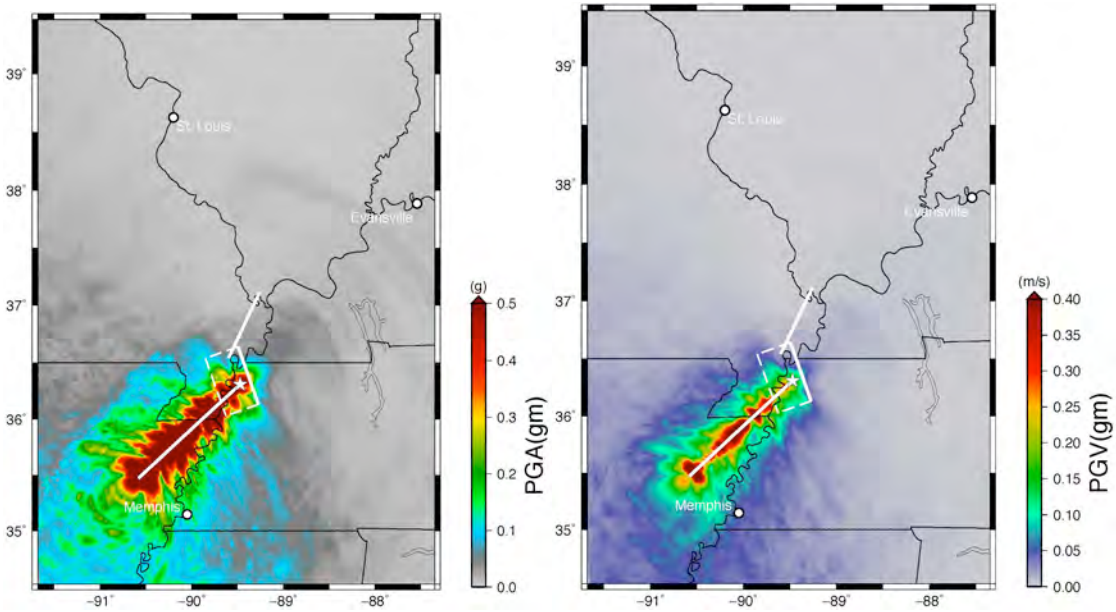

Figure 13. Same as Figure 10, but for a uni-lateral rupture from NE on the SW segment.

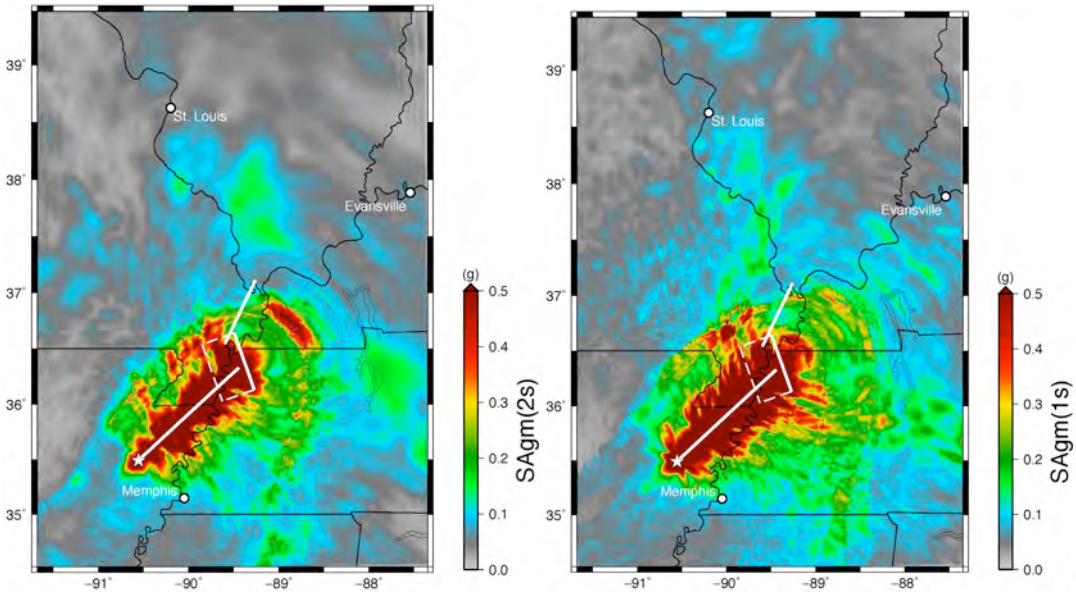

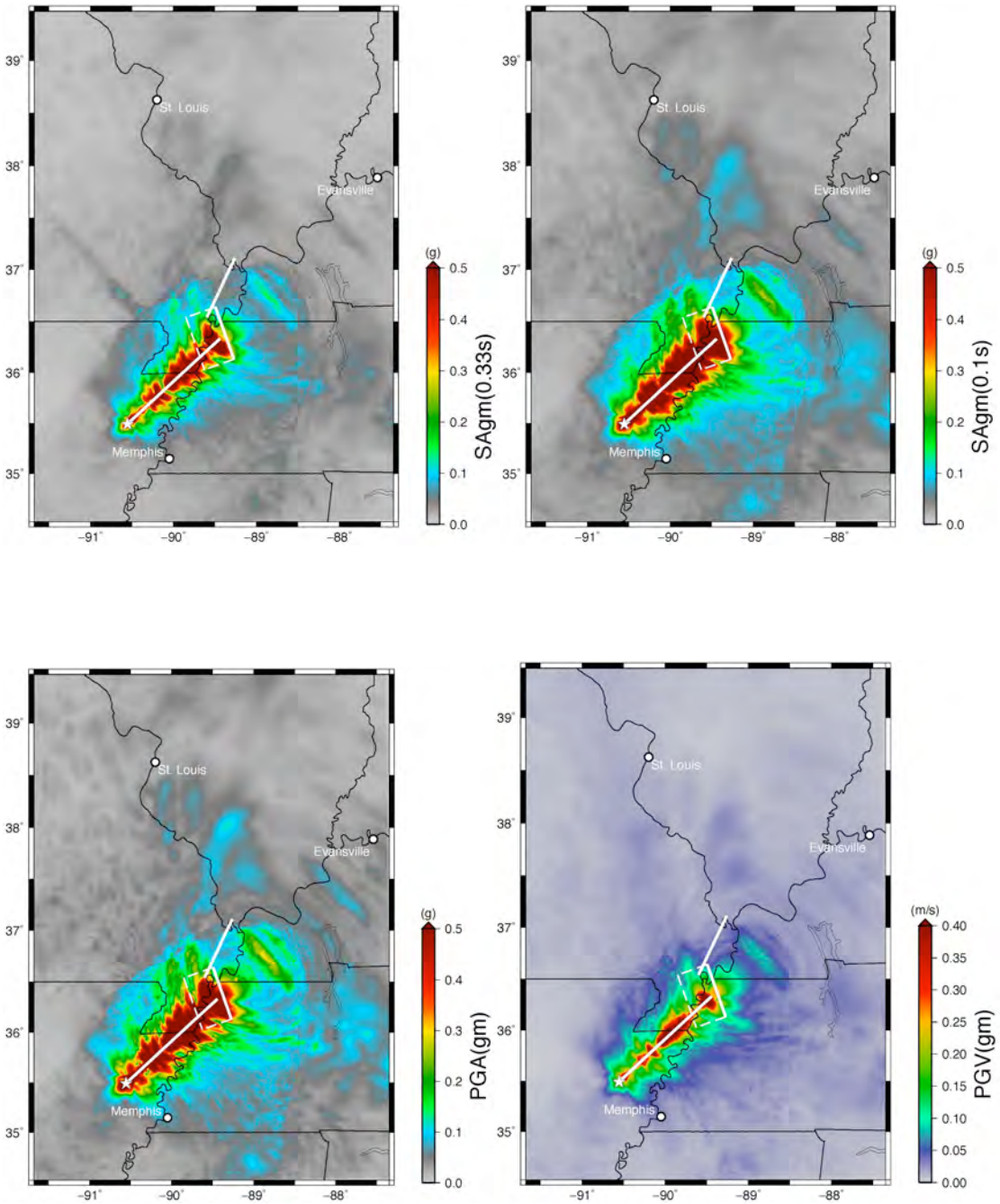

Figure 14. Same as Figure 13, but for a uni-lateral rupture from SW on the SW segment.

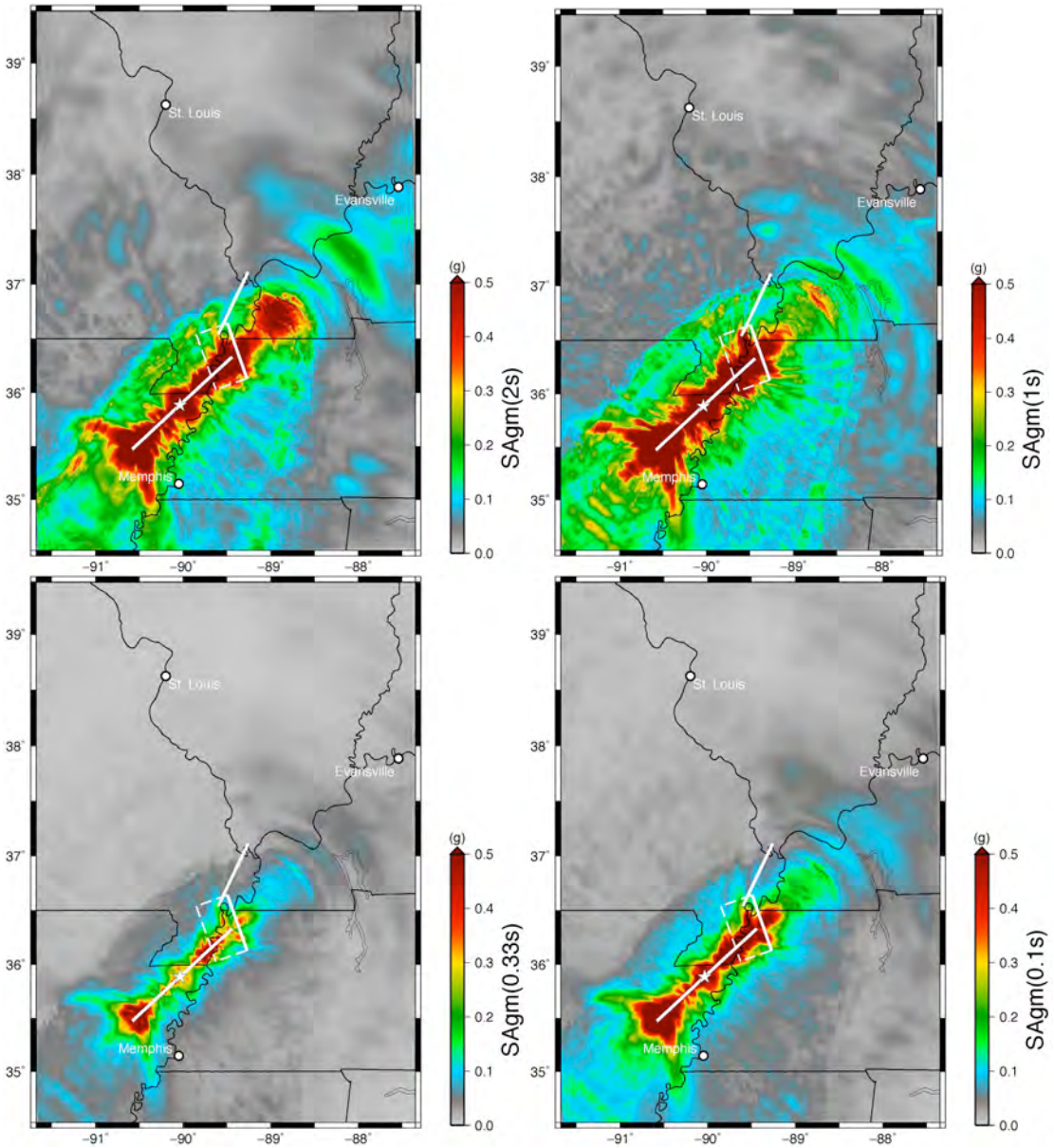
St. Louis
Evansville
Memphis
39°
38°
37°
36°
35°
−91°
−90°
−89°
−88°
(g)
0.5
0.4
0.3
0.2
0.1
0.0
SAgm(2s)
SAgm(1s)
SAgm(0.33s)
SAgm(0.1s)

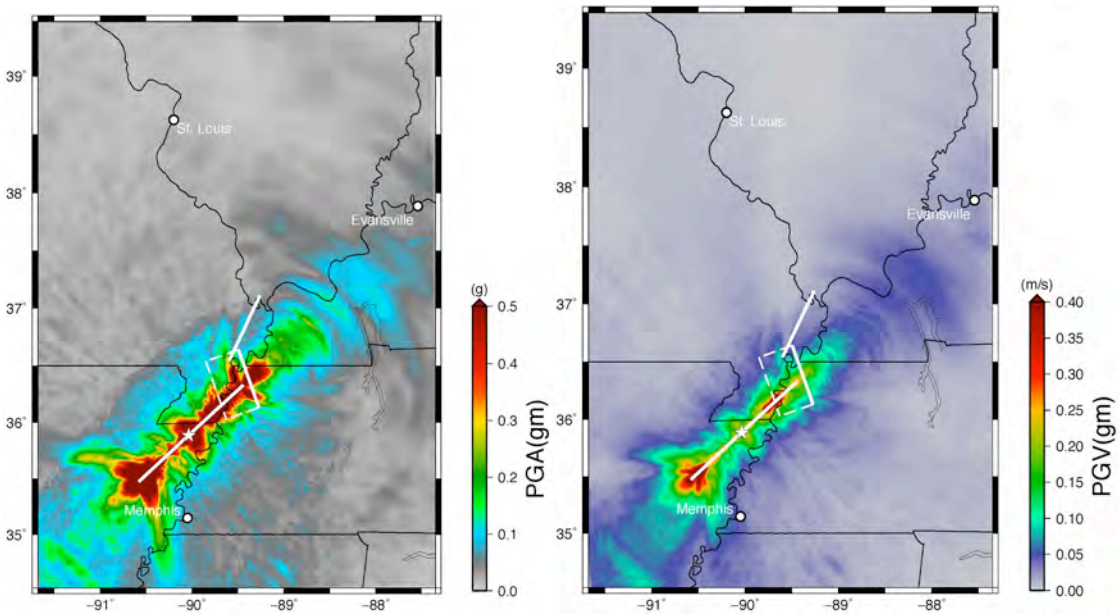

Figure 15. Same as Figure 13, but for a bi-lateral rupture on the SW segment.

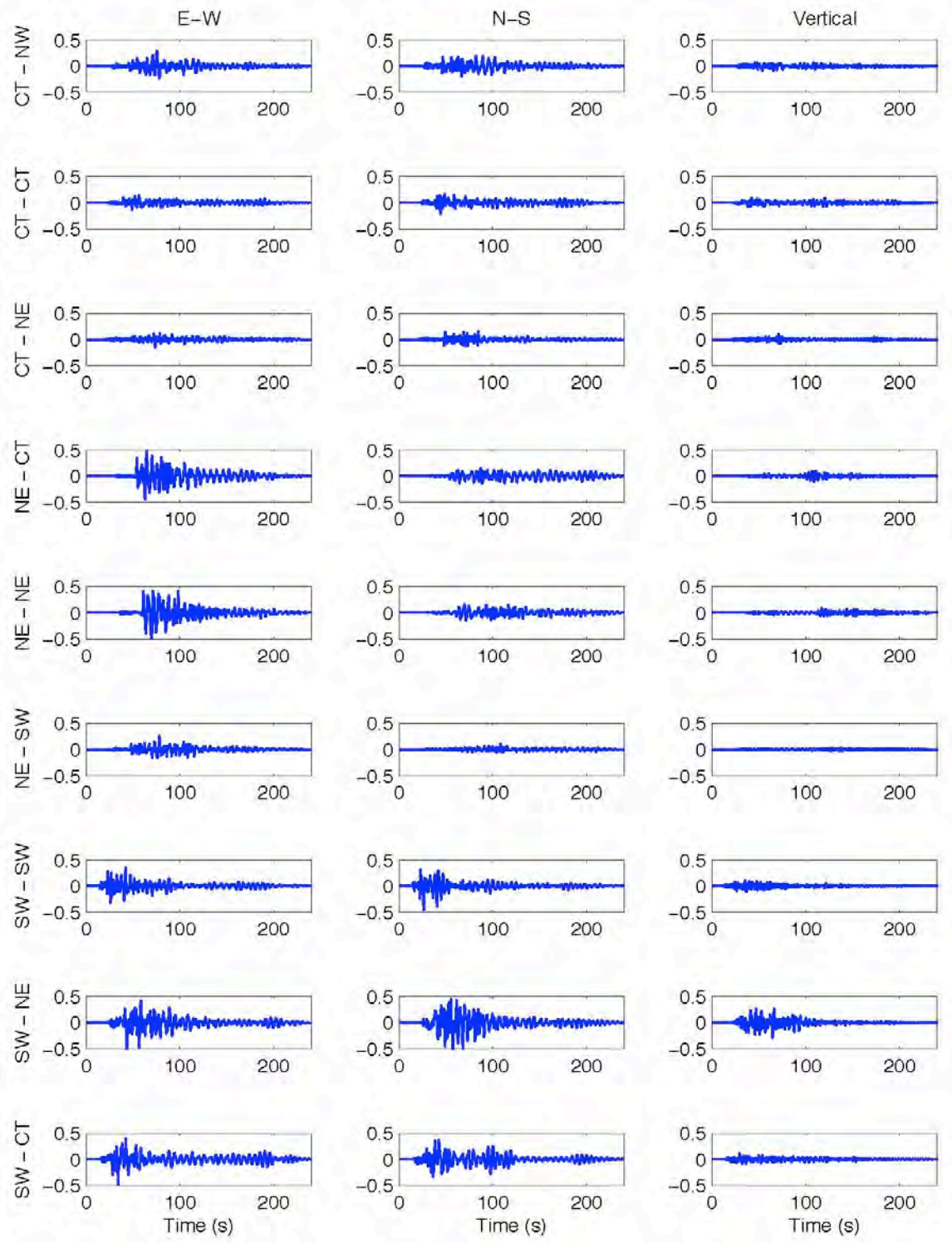

Figure 16. BB velocity seismograms (m/s) at Memphis for each of the 9 scenario earthquakes. The abbreviation on the left indicates the rupture segment (CT=central, NE=northeast, and SW=southwest) followed by the epicentral location (NW=northwest, CT=central, NE=northeast, SW=southwest).

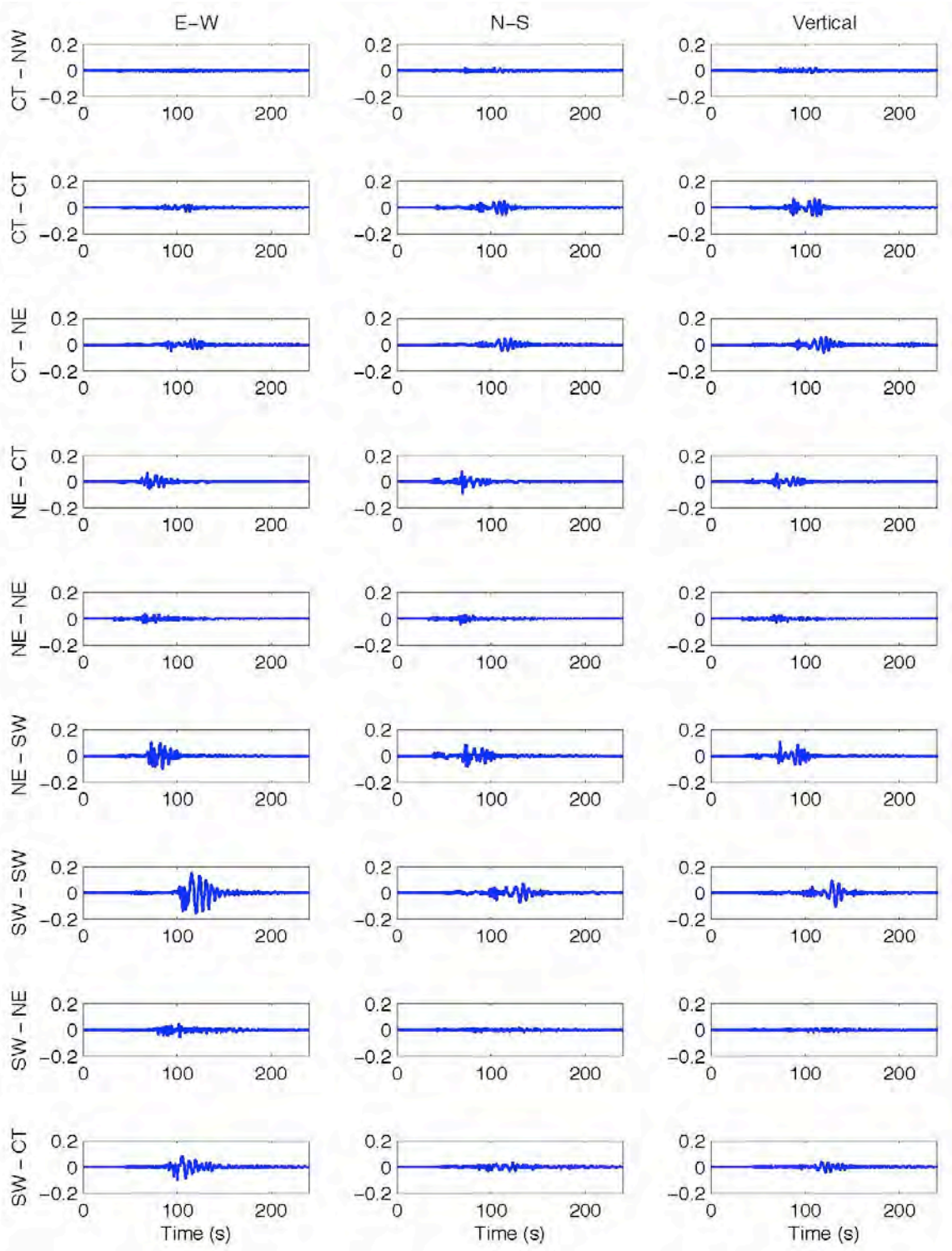

Figure 17. Same as Figure 16, but for St Louis, MO.